

RESEARCH ARTICLE

10.1002/2016GB005485

Key Points:

- Pacific C_{anth} increased by 6.1 ± 1.5 PgC between 90s and 2000s and by 8.8 ± 2.2 PgC between the 2000s and 2010s
- Novel ensemble eMLR can resolve and reduce uncertainties from regression coefficient choices
- C_{anth} uptake increased in the Southern Pacific in the recent decade, likely due to enhanced Pacific Subtropical Cell ventilation

Supporting Information:

- Supporting Information S1
- Data Set S1
- Movie S1

Correspondence to:

B. R. Carter,
brendan.carter@noaa.gov

Citation:

Carter, B. R., et al. (2017), Two decades of Pacific anthropogenic carbon storage and ocean acidification along Global Ocean Ship-based Hydrographic Investigations Program sections P16 and P02, *Global Biogeochem. Cycles*, 31, 306–327, doi:10.1002/2016GB005485.

Received 25 JUL 2016

Accepted 17 JAN 2017

Accepted article online 21 JAN 2017

Published online 10 FEB 2017

©2017. The Authors.

This is an open access article under the terms of the Creative Commons Attribution-NonCommercial-NoDerivs License, which permits use and distribution in any medium, provided the original work is properly cited, the use is non-commercial and no modifications or adaptations are made.

Two decades of Pacific anthropogenic carbon storage and ocean acidification along Global Ocean Ship-based Hydrographic Investigations Program sections P16 and P02

B. R. Carter^{1,2} , R. A. Feely², S. Mecking³ , J. N. Cross², A. M. Macdonald⁴ , S. A. Siedlecki¹ , L. D. Talley⁵ , C. L. Sabine² , F. J. Millero⁶ , J. H. Swift⁵, A. G. Dickson⁵ , and K. B. Rodgers⁷

¹Joint Institute for the Study of the Atmosphere and Ocean, University of Washington, Seattle, Washington, USA, ²NOAA Pacific Marine Environmental Laboratory, Seattle, Washington, USA, ³Applied Physics Laboratory, University of Washington, Seattle, Washington, USA, ⁴Woods Hole Oceanographic Institution, Woods Hole, Massachusetts, USA, ⁵Scripps Institution of Oceanography, University of California, San Diego, La Jolla, California, USA, ⁶Rosenstiel School of Marine and Atmospheric Science, University of Miami, Coral Gables, Florida, USA, ⁷Atmospheric and Oceanic Sciences Program, Princeton University, Princeton, New Jersey, USA

Abstract A modified version of the extended multiple linear regression (eMLR) method is used to estimate anthropogenic carbon concentration (C_{anth}) changes along the Pacific P02 and P16 hydrographic sections over the past two decades. P02 is a zonal section crossing the North Pacific at 30°N, and P16 is a meridional section crossing the North and South Pacific at ~150°W. The eMLR modifications allow the uncertainties associated with choices of regression parameters to be both resolved and reduced. C_{anth} is found to have increased throughout the water column from the surface to ~1000 m depth along both lines in both decades. Mean column C_{anth} inventory increased consistently during the earlier (1990s–2000s) and recent (2000s–2010s) decades along P02, at rates of 0.53 ± 0.11 and 0.46 ± 0.11 mol C m⁻² a⁻¹, respectively. By contrast, C_{anth} storage accelerated from 0.29 ± 0.10 to 0.45 ± 0.11 mol C m⁻² a⁻¹ along P16. Shifts in water mass distributions are ruled out as a potential cause of this increase, which is instead attributed to recent increases in the ventilation of the South Pacific Subtropical Cell. Decadal changes along P16 are extrapolated across the gyre to estimate a Pacific Basin average storage between 60°S and 60°N of 6.1 ± 1.5 PgC decade⁻¹ in the earlier decade and 8.8 ± 2.2 PgC decade⁻¹ in the recent decade. This storage estimate is large despite the shallow Pacific C_{anth} penetration due to the large volume of the Pacific Ocean. By 2014, C_{anth} storage had changed Pacific surface seawater pH by -0.08 to -0.14 and aragonite saturation state by -0.57 to -0.82 .

1. Introduction

Since the beginning of the Industrial Era, the global ocean has absorbed approximately 28% of the anthropogenic carbon dioxide (C_{anth}) emissions released into the atmosphere from fossil fuel burning, land use changes, and cement production [Canadell et al., 2007; Le Quéré et al., 2015]. As of 1994, ~38% of this oceanic C_{anth} resided in the Pacific [Sabine et al., 2002, 2004]. Ocean CO₂ uptake is significant for Earth's climate and ecosystems for several reasons. Atmospheric CO₂ traps heat in the Earth system, while marine CO₂ does not, so ocean storage has slowed anthropogenic global warming and warming-induced intensification of the hydrological cycle [Durack et al., 2012]. Ocean CO₂ uptake also reduces seawater pH and carbonate ion concentrations [CO₃²⁻]. This ocean acidification is thought likely to have far-reaching impacts on ocean ecosystems, particularly on organisms that utilize CO₃²⁻ to form their shells and hard parts [Doney et al., 2009; Pfister et al., 2014; Gattuso et al., 2015; Gattuso and Feely, 2016]. Consequently, monitoring carbon and anthropogenic carbon concentrations in the Pacific and the other major ocean basins is a critical task for Earth scientists.

Sabine et al. [2004] estimated global ocean C_{anth} distributions from the 1990s World Ocean Circulation Experiment (WOCE) measurements. Their approach was to subtract estimates of natural carbon concentrations, meaning the carbon that would be expected in the absence of anthropogenic CO₂ emissions, from total dissolved inorganic carbon concentrations (C_T). Scientists have more recently used time histories of contact between seawater and the atmosphere inferred from other tracer measurements (e.g., through the transit time distribution and maximum entropy methods of Waugh et al. [2006] and Khatiwala et al.

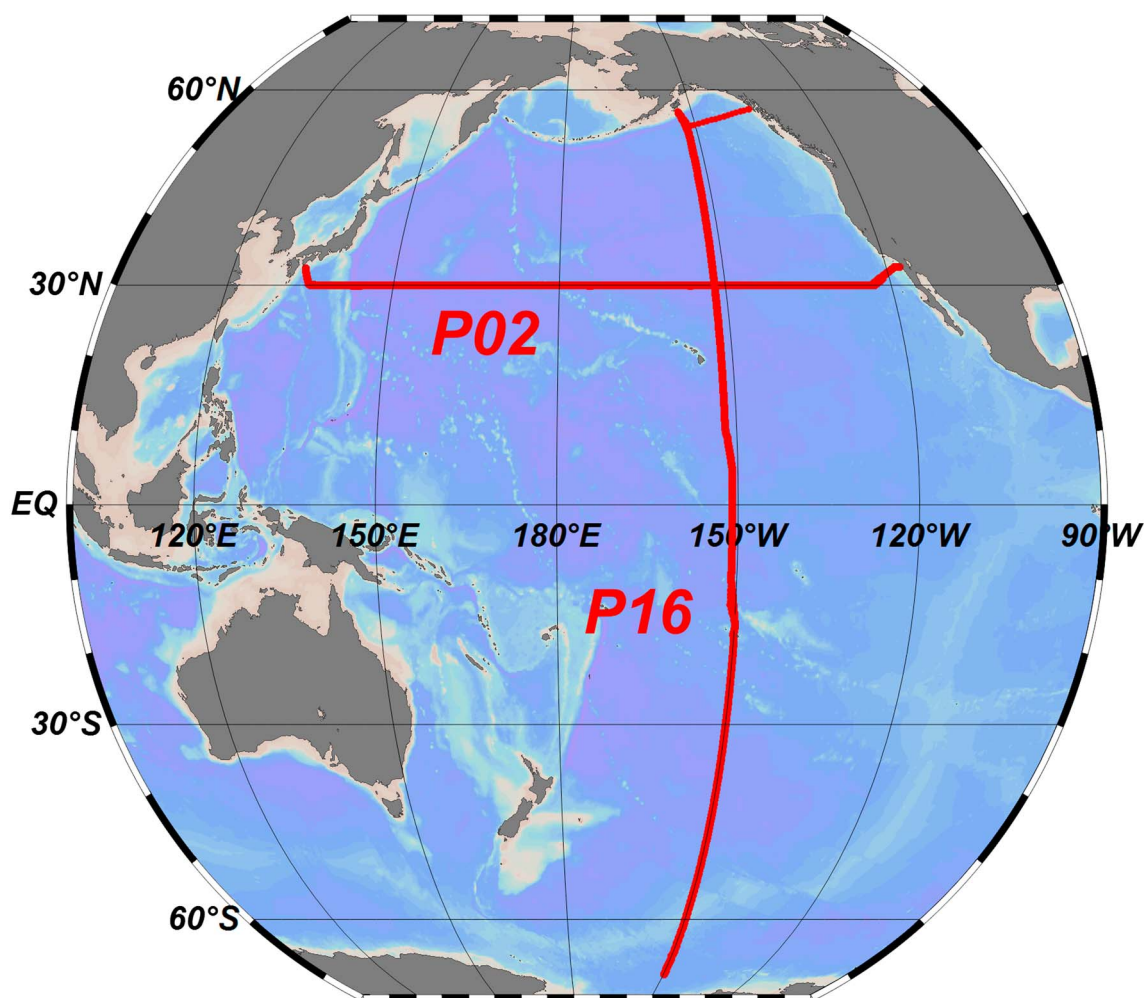


Figure 1. A map of the P02 and P16 sections in the Pacific.

[2009]). These methods provide C_{anth} estimates from individual synoptic surveys, but the methods rely on uncertain assumptions regarding the consistency of water mass ventilation pathways or the shapes of water mass age distributions. In recent decades, the Repeat Hydrography program, a contribution to the U.S. Climate Variability and Predictability (CLIVAR) program, and the more recent international Global Ocean Ship-based Hydrographic Investigations Program (GO-SHIP), repeated a subset of the measurements made along the WOCE hydrographic lines on decadal intervals. These repeated hydrographic transects provide valuable independent information as they allow direct estimation of decadal changes in carbon inventories without relying on the assumptions used by other methods.

Decadal changes in C_T cannot be solely attributed to anthropogenic carbon uptake due to large natural variability in ocean C_T . Wallace [1995] proposed a multiple linear regression (MLR) approach to address the part of these C_T fluctuations resulting from natural variability. This method and the more commonly used extended MLR (eMLR) [Friis *et al.*, 2005] variant, which is described in greater detail in section 2, parameterize the influences of natural variability using regressions of C_T against other measured properties. The regressions from one occupation are combined with the measurements from another occupation to estimate the C_T distribution expected if natural variability had been identical in both cases. Differences between measured and expected C_T distributions are then attributed to C_{anth} concentration changes. The eMLR method has been used extensively to quantify decadal ocean C_{anth} changes [e.g., Sabine *et al.*, 2008; Wanninkhof *et al.*, 2010; Williams *et al.*, 2015; Chu *et al.*, 2016; Woosley *et al.*, 2016]. The method has been tested in biogeochemical ocean circulation models with known C_{anth} distributions and shown to be capable of reproducing known modeled regionally averaged anthropogenic carbon inventory changes to within 20% when used

Table 1. Cruise Expocodes, Years, and Adjustments Applied to the Later Data Set in Each Comparison^a

Expocode	Section	Year	<i>T</i>	<i>S</i>	<i>O</i> ₂	<i>N</i>	<i>Si</i>	<i>C</i> _T	<i>A</i> _T	
			Offset Adjustments			Multiplier Adjustments				
			(°C)		(μmol kg ⁻¹)					
316N138_9 ^b	P16S	1992	-	-	-	-	-	-	-	
31WTTUNES_2 ^b	P16C	1991	-	-	-	-	-	-	-	
31WTTUNES_3 ^b										
31DSCGC91_1 ^b	P16N	1992	-	-	-	-	-	-	-	
49K6KY9401_1	P02E	1994	-	-	-	-	-	-	-	
49K6KY9401_1	P02W	1994	-	-	-	-	-	-	-	
33RR200501	P16S	2005	0.071	0.001	-0.8	0.9948	0.9921	1.0003	0.9985	
325020060213	P16C	2006	-0.068	0.003	-1.6	1.0086	0.9869	1.0001	1.0003	
325020060213	P16N	2006	0.009	0.006	-2.8	0.9969	0.9810	1.0001	1.0008	
318 M200406	P02E	2004	0.054	-0.013	-1.0	1.0089	0.9892	0.9993	1.0043	
318 M200406	P02W	2004	0.056	-0.024	-1.9	1.0220	0.9888	0.9988	1.0057	
320620140320	P16S	2014	0.065	-0.003	-0.3	1.0008	0.9964	1.0000	1.0003	
33RO20150410	P16C	2015	0.065	-0.003	-1.7	0.9888	0.9874	0.9996	0.9988	
33RO20150525	P16N	2015	0.007	0.002	-1.1	1.0059	0.9890	1.0006	0.9988	
318 M20130321	P02E	2013	-0.083	-0.006	-0.7	0.9999	1.0064	1.0005	0.9994	
318 M20130321	P02W	2013	0.006	0.002	-0.3	0.9954	1.0020	1.0003	0.9982	

^aAll cruise data were acquired from the CLIVAR and Carbon Hydrographic Data Office (CCHDO) data portal.

^bThe cruises where data were extracted data from the GLODAPv1.1 data product of [Key *et al.*, 2004]. This data product calculated *A*_T from diverse carbonate system parameters when unmeasured.

judiciously [Levine *et al.*, 2008; Goodkin *et al.*, 2011; Plancherel *et al.*, 2013]. However, eMLR estimate uncertainties are larger at specific locations due in large part to semiarbitrary decisions concerning the particular parameters to include in the regressions [Plancherel *et al.*, 2013]. In this study, we use the eMLR approach to estimate decadal *C*_{anth} storage along the Pacific P16 and P02 sections (Figure 1) between the early 1990s and 2000s (WOCE to CLIVAR) and between the 2000s and the modern decade (CLIVAR to GO-SHIP). We therefore repeat and extend some of the work of Sabine *et al.* [2008], who also considered Pacific *C*_{anth} accumulation between the 1990s and 2000s along the P02 and P16 sections. Several novel modifications to the method are used (section 2.2) to reduce the impact of decisions required for eMLR on the estimated *C*_{anth} values.

2. Methods

2.1. Data Used

Samples were collected along P02 (~30°N) and P16 (~150°W) (Figure 1) on 16 cruise legs over three decades. Cruise stations were typically separated by 30 nautical miles along the lines, and up to 24–36 samples were measured from the ocean surface to the ocean bottom per station. *C*_T was measured on these samples, allowing us to estimate *C*_{anth} storage for the ~20 years spanning these sets of measurements. The P02 and P16 transects are chosen because they each have three completed occupations. We refer to the six 1990s WOCE era cruise legs as “early” cruises, the five 2000s CLIVAR era cruise legs as “middle” cruises, the five GO-SHIP era 2010s cruise legs as “recent” cruises (cruise Expocodes are provided in Table 1), and the decades spanning these reoccupations as the “earlier” and recent decades.

Measurements of temperature (*T*), salinity (*S*), oxygen concentration (*O*₂), total nitrate and nitrite concentration (*N*), and total silicate concentration (*Si*) are used in this analysis in addition to *C*_T. Total seawater titration alkalinity (*A*_T) is used as a second carbonate system constraint to calculate *pCO*₂ in the mixed layer. We do not include *A*_T as a regression parameter due to relatively large adjustments required for deep data consistency. Initial experimentation that did include *A*_T returned qualitatively similar results but with increased estimate noise. Phosphate concentrations are similarly not used in the regressions because there are large deep water phosphate changes along P02 between WOCE and CLIVAR, possibly indicating measurement offsets between cruises. Also, since phosphate and *N* have similar distributions, including phosphate with *N* adds little independent information to the regressions and brings along the risk of over fitting *C*_T.

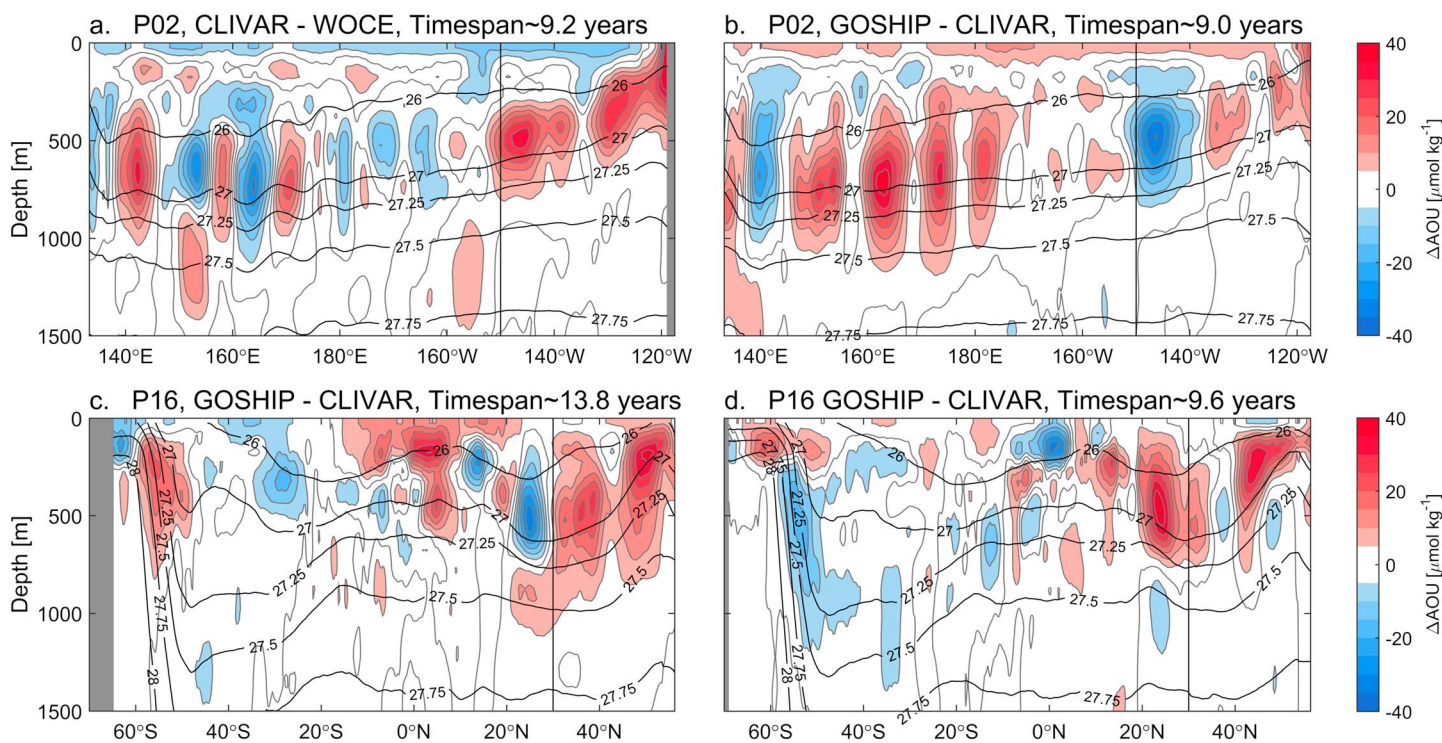


Figure 2. Sections of direct Pacific C_T changes. Sections are (a) P02 (east-west at $\sim 30^\circ\text{N}$) in the earlier decade, (b) P02 in the recent decade, (c) P16 (north-south at $\sim 150^\circ\text{W}$) in the earlier decade, and (d) P16 in the recent decade. Vertical black lines indicate crossovers between the two sections, and curved black lines indicate surfaces of constant γ^N .

Several steps were taken to prepare the data sets for analysis. First, data flagged in the data sets as questionable or bad are omitted, along with fewer than 10 (out of $\sim 33,000$ total property measurements) apparent C_T outlier measurements that appear as “bull’s-eyes” in contour plots. Second, as Pacific Ocean properties are not expected to experience strong changes between 3000 and 4000 m depth (i.e., in Pacific deep water) on decadal timescales, adjustments (Table 1) are applied to the later data set in each comparison to counter any differences observed at these depths. While we believe that the adjustments applied are appropriate, we account for the possibility that the adjustments are countering real shifts in water mass properties in our error assessment (Appendix A). For T , S , and O_2 , adjustments are applied by subtracting the mean property change over this depth range from all later occupation data. For N , Si , C_T , and A_T the later occupations are divided by the ratio of the mean deep values in the later occupations to the mean values in the earlier occupations. The choice between fixed offsets and multiplicative adjustments was made on a property-by-property basis in light of the kinds of errors that are likely to arise during the measurement analyses. A fixed offset was used when uncertain.

Potential temperature (θ), potential density (σ_θ), and apparent oxygen utilization (AOU, equivalent to the oxygen deficit relative to atmospheric equilibrium) were calculated using the seawater routines for MATLAB [Morgan and Pender, 2006]. Neutral density (γ^N) was calculated using the routines from Jackett and McDougall [1997].

2.2. Estimating Decadal C_{anth} Change

Before C_{anth} can be estimated, the impacts of natural variability need to be removed from changes in C_T . These modes of variability include shifts in the locations of water masses on subdecadal timescales and variability in biogeochemical cycling patterns. The impacts of these modes of variability and ongoing C_{anth} uptake can be seen in large and spatially variable decadal C_T (Figure 2) and AOU (Figure 3) changes along P02 and P16. We use the eMLR approach to remove the impacts of variability from these measurement change distributions.

The eMLR approach assumes that the natural processes changing C_T also change other measurable seawater properties that are unaffected by C_{anth} uptake. For instance, shifts in water mass locations affect most

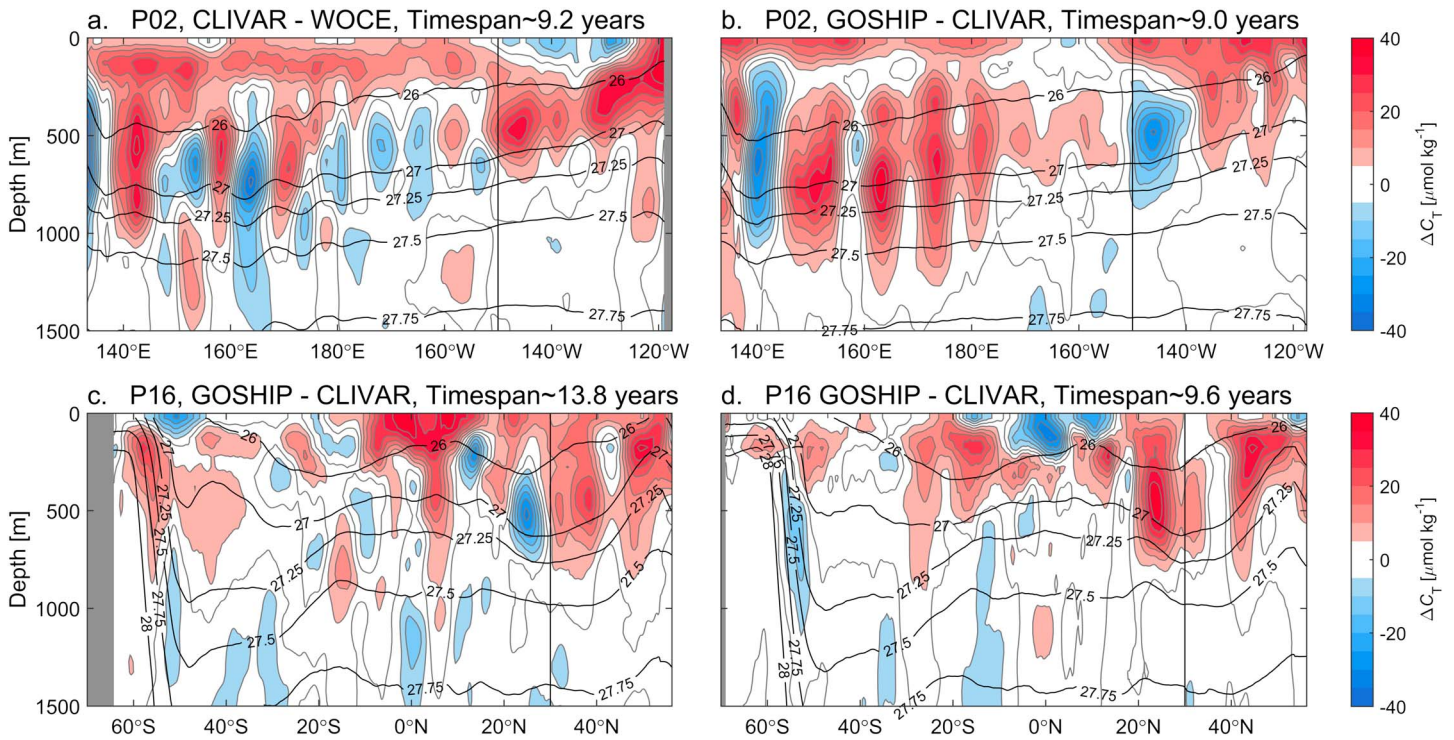


Figure 3. Sections of direct Pacific AOU changes. Sections are (a) P02 (east-west at ~30°N) in the earlier decade, (b) P02 in the recent decade, (c) P16 (north-south at ~150°W) in the earlier decade, and (d) P16 in the recent decade. Vertical black lines indicate crossovers between the two sections, and curved black lines indicate surfaces of constant γ^N .

measured properties, and variability in biogeochemical cycling affects N , Si , and AOU distributions as well as C_T . The first step in the eMLR approach involves creating empirical linear functions “ f ” from the other measured (e.g., S , N , and Si) and derived (e.g., θ and AOU) properties “ P ” to capture the effect of natural variability on C_T (equation (1)) as follows:

$$f(P) = C_T \tag{1}$$

Then the function from each decade is applied to the same set of measurements to yield estimates of what the measured C_T would have been had the modes of natural variability acted identically during both occupations. The differences between these estimates are then the portions of C_T changes that are not accounted for by natural variability, which are therefore attributed to C_{anth} uptake (equation (2)). For the earlier decade, this is expressed as follows:

$$C_{anth} = f_2(P_2) - f_1(P_2) \tag{2}$$

In these equations the subscripts indicate the decades the terms are specific to, with 1 and 2 being the early and middle decades, respectively. The recent decade is later denoted with a 3.

Goodkin et al. [2011] warn eMLR users that circulation changes will render the empirical relationships determined for an earlier decade unsuitable for reproducing variability in a later decade when reoccupations are separated by 30 years or more, and *Plancherel et al.* [2013] show that bias can be introduced when the sampling network is inconsistent between reoccupations. However, we only consider overlapping portions of sections with maximum reoccupation intervals of 15 years, so neither of these cautions applies to our work.

We use several modifications to the eMLR approach to isolate C_{anth} storage changes from natural C_T variability. Modifications are listed here and details follow. Assertions about the efficacy of these modifications are based on tests detailed in Appendix B.

1. As done by *Friis et al.* [2005], we compare C_T estimates from regressions to one another (equation (2)) rather than directly to the measurements (i.e., we use eMLR, not MLR), thereby canceling a portion of the C_T fit error.

Table 2. Properties Used in Each of the 16 Regressions for C_T^a

Regression Number	i_θ	i_S	i_{AOU}	i_N	i_{Si}
1	1	1	1	0	0
2	1	1	0	1	0
3	1	1	0	0	1
4	1	0	1	1	0
5	1	0	1	0	1
6	1	0	0	1	1
7	0	1	1	1	0
8	0	1	1	0	1
9	0	1	0	1	1
10	0	0	1	1	1
11	1	1	1	1	0
12	1	1	1	0	1
13	1	1	0	1	1
14	1	0	1	1	1
15	0	1	1	1	1
16	1	1	1	1	1

^a"1" indicates the property is used and a "0" indicates it is not. AOU is regressed only for the five regressions with i_{AOU} of 0.

2. As done by *Sabine et al.* [2008], we include an adjustment based on AOU changes to account for potential additional changes in biogeochemical C_T cycling that are not resolved by the eMLR regressions. We find that this adjustment decreases mean estimate error and RMS error by ~7–15%.
3. As done by *Velo et al.* [2013] for A_T regressions, we use "robust" multiple linear regression. Robust regression minimizes the impact of outliers on our regressions by iteratively reestimating regression coefficients after assigning smaller weights to measurements with larger residuals, thereby excluding outliers. We use the "robustfit" MATLAB robust regression routine with a bisquare outlier test and the recommended default turning constant, meaning data with residuals in excess of 4.685 times the standard residuals are given no weight.
4. Like *Velo et al.* [2013] and *Carter et al.*, 2016a, we use a moving window in depth, γ^N , and latitude or longitude to select data for each regression. This moving window removes the need to make arbitrary decisions regarding which depth or density intervals to use for each regression and reduces the number of independent variables required to capture the modes of variability along hydrographic sections bisecting many heterogeneous water masses. Omitting the moving window doubles mean errors, though most error increase occurs when omitting the moving window in depth/density, and many previous studies have included multiple regressions for various depth ranges. Omitting the horizontal component of the moving window only improves mean error by ~10%. Neither window has a strong impact on RMS error. The primary advantage the moving window offers is eliminating the need for choices regarding how to partition the water column vertically.
5. Finally, we use 16 combinations (Table 2) of our five regression seawater properties (θ , S , AOU, S_i , and N) for our regressions and use the mean C_{anth} estimate returned by these varied regressions as our final C_{anth} estimates. *Plancherel et al.* [2013] tested various approaches for reconstructing known simulated C_{anth} distributions and showed that the choice of which properties to include in a regression can have a substantial impact on the C_{anth} estimates returned. Their mean estimate was also somewhat better than the estimate from the best Akaike information criterion approach, which scrupulously chose the regression parameter combination with the best fit relative to the number of degrees of freedom for several depth intervals. We find that this adjustment decreases our mean estimate errors by ~30–40% and RMS errors by ~60–80%.

We are unaware of steps 3 through 5 being used for eMLR ΔC_{anth} estimates before. We refer to our approach as an "ensemble eMLR" because of step 5.

The first step of the ensemble eMLR method is to select "local" data for each of our 33,000+ regression locations by applying moving windows around each data point (one for each measured location in each data set). Local data are data remaining after excluding all measurements as follows: (1) within the mixed layer (more below), (2) more than 15° of latitude or longitude away, (3) found on a different hydrographic line than the location (i.e., along P02 versus P16), and (4) that are both more than 200 m deeper or shallower and either $0.1 \text{ kg m}^{-3} \gamma^N$ denser or less dense than the density of the seawater for which regression constants are being determined.

Requirement 4 is designed to have the local data window rely on γ^N , but it also includes a depth threshold to ensure the inclusion of enough measurements to constrain a regression within regions of large vertical

density gradients. An average of 303 measurements is used per regression with these criteria. The WOCE P02 section has lower measurement density than the other sections, and one regression is performed with as few as 10 sets of measurements between 1100 and 1300 m depth. Regressions with so few measurement sets are suspect, so we also repeat all calculations with the windows used for requirements 2 and 3 doubled in size for the earlier P02 comparison. We present the findings from the undoubled windows for comparability but note the finding that is not robust between the two treatments. Aside from this subsection of WOCE P02, the minimum number of measurement sets used in a single regression is 45 along the WOCE P16 line. With doubled window sizes, the minimum number of measurement sets used along the P02 line is also 45.

Next, the regression coefficients are estimated for C_T . The general form of the equation fit to data is as follows:

$$C_T = \alpha_1^1 + i^\theta \alpha_1^\theta \theta + i^S \alpha_1^S S + i^N \alpha_1^N N + i^{Si} \alpha_1^{Si} Si + i^{AOU} \alpha_1^{AOU} AOU \quad (3)$$

In equations (3) and (4), the α values are the regression coefficients. Superscripts link coefficients to their associated predictors, and subscripts refer to occupations (as before). The i terms are either values of 1 or 0 depending on whether the specific regressions contain each of the five properties (see Table 2). Regression coefficients are similarly estimated for AOU for the five regressions that omit AOU as a predictor variable as follows:

$$AOU = \beta_1^1 + i^\theta \beta_1^\theta \theta + i^S \beta_1^S S + i^N \beta_1^N N + i^{Si} \beta_1^{Si} Si \quad (4)$$

β regression coefficients are estimated at every location for which there are C_T measurements in the early, middle, and recent data sets. These regressions implicitly include latitude/longitude and depth as regression coefficients by virtue of allowing the fits to change in space. It is possible to obtain smaller regression residuals using fits with more regression parameters. However, the strength of regression fits has been shown to be a poor indicator of eMLR skill, and including more regression parameters increases the risk of overfitting the signal. We therefore consider estimates from each of these 16 regressions to be equally likely. For discussion purposes only, a seventeenth regression is performed using only θ and S .

The next step in the process is to grid the regression coefficients from the paired data sets onto a regular 2-D depth longitude grid. Properties are gridded vertically onto every 50 m increment between 25 m and 5475 m depth using the cubic Hermite piecewise polynomial linear interpolation scheme described by *Carter et al.* [2014] (supporting information S1). Seawater properties and regression coefficients are then linearly interpolated onto every quarter degree of longitude and latitude along the two sections. All further analyses are carried out using these gridded values. However, for figure clarity, data are smoothed using a $\pm 1^\circ$ latitude or longitude averaging window centered on each grid point before plotting sections.

The residual portions of AOU and C_T water mass changes that are not captured by the regressions (r_{AOU} and r_C) are estimated at each grid location for each regression by differencing the interpolated regression coefficients according to equations (5) and (6) and multiplying by the property distributions as follows:

$$r_C = (\alpha_2^1 - \alpha_1^1) + i_\theta (\alpha_2^\theta - \alpha_1^\theta) \theta + i_S (\alpha_2^S - \alpha_1^S) S + i_{AOU} (\alpha_2^{AOU} - \alpha_1^{AOU}) AOU + i_N (\alpha_2^N - \alpha_1^N) N + i_{Si} (\alpha_2^{Si} - \alpha_1^{Si}) Si \quad (5)$$

$$r_{AOU} = (\beta_2^1 - \beta_1^1) + i_\theta (\beta_2^\theta - \beta_1^\theta) \theta + i_S (\beta_2^S - \beta_1^S) S + i_{AOU} (\beta_2^{AOU} - \beta_1^{AOU}) AOU + i_N (\beta_2^N - \beta_1^N) N + i_{Si} (\beta_2^{Si} - \beta_1^{Si}) Si \quad (6)$$

Equation (6) is only applied to the five regressions lacking AOU as a predictor variable (Table 2). Except when otherwise specified, the property values used to estimate these changes are from the later occupation of each pair. We caution that r_{AOU} estimates are not equivalent to AOU changes at a location (ΔAOU), as a portion of ΔAOU will correlate with the regression parameters and be removed by equation (6) (see also section 3.1).

Following *Sabine et al.* [2008], the portion of r_C attributable to changes in net biological remineralization (ΔC_{bio}) was estimated as the product of ΔAOU and a remineralization ratio [*Anderson and Sarmiento, 1994*] as follows:

$$\Delta C_{\text{bio}} = r_{\text{AOU}} \frac{117 \text{ } \mu\text{mol C}}{170 \text{ } \mu\text{mol O}_2} \quad (7)$$

For the five regressions without AOU, this term is subtracted from r_C to adjust for redistribution of C_T from remineralized organic matter—either through changes in biological cycling or circulation—that is not adequately captured by regressions with other properties (e.g., S , θ , N , and Si) in equation (5). For the 11 regressions with AOU, r_{AOU} , and ΔC_{bio} are exactly 0. The remainder of the r_C signal is attributed to anthropogenic carbon uptake (ΔC_{anth}) according to equation (8) as follows:

$$\Delta C_{\text{anth}} = r_C - \Delta C_{\text{bio}} \quad (8)$$

A similar adjustment could be made using “ r_A ,” defined analogously to ΔAOU and ΔC_T , to capture unresolved C_T changes from shifts in the calcium carbonate cycling. However, early experimentation revealed that an adjustment based on r_A had little net effect (suggesting that these changes are small or well captured by regression with N , AOU, or Si) and resulted in noisier estimates at all depths.

Sabine et al. [2008] argue that the eMLR treatment is unreliable and unnecessary in the mixed layer where strong biological cycling and gas exchange decouple water mass properties and where C_{anth} increases approximately track atmospheric increases. We therefore exclude measurements in water shallower than the deepest monthly mixed layer in the mixed layer climatology of Holte et al. (accessed Nov. 2014) from eMLR. For the mixed layer, which is better equilibrated with the atmosphere than deeper layers, anthropogenic storage is estimated in several steps. We (1) estimate $p\text{CO}_2$ for the later occupation from A_T , C_T , and carbonate constants [Dickson and Millero, 1987]; (2) subtract the increase in annual mean atmospheric $p\text{CO}_2$ between the earlier and later occupations according to the Mauna Loa observatory record [Keeling, 1986]; (3) estimate C_T using the A_T measured during the later occupation and the diminished $p\text{CO}_2$; and (4) assume that the anthropogenic storage is equal to the difference between the measured C_T and this lower C_T estimate.

These steps produce a ΔC_{anth} estimate at each grid location for both decades considered for each of the 16 regressions. These 16 estimates are then averaged for the final ΔC_{anth} distribution estimates. We forgo performing a weighted average because there is no solid a priori basis from which to determine weights for the regressions.

2.3. Column Inventory Change, Basin Storage, and Overall C_{anth} Estimates

C_{anth} column inventory changes are estimated in $\text{mol C m}^{-2} \text{a}^{-1}$ by summing ΔC_{anth} over depth and dividing by the years between reoccupations. We sum from the surface to depth at which the mean ΔC_{anth} across latitude or longitude is $0.5 \text{ } \mu\text{mol kg}^{-1}$. This threshold is smaller than typical uncertainties for individual estimates ($3\text{--}5 \text{ } \mu\text{mol kg}^{-1}$; see Appendix A) because we are averaging across the large number of estimates obtained at each station along a line, each of which has partially independent uncertainties. Thresholds between 0 and $1 \text{ } \mu\text{mol kg}^{-1}$ return similar average results. Higher thresholds yield consistently smaller column inventory estimates, and lower thresholds return greater variability among estimates from different regressions.

Basin-scale storage is estimated using the gridded World Ocean Atlas annual mean temperature and salinity data product [Locarnini et al., 2013; Zweng et al., 2013]. First, potential density σ_θ is calculated for each of the gridded data product locations. Next, C_{anth} changes at each location are estimated as the ΔC_{anth} on the same σ_θ surface at the same latitude along P16, normalized to a 10 year time change. The overall change is estimated as the grid cell volume-weighted sum of the ΔC_{anth} . This estimate uses only P16 because the asymmetry of the gyres in the Northern and Southern Hemispheres suggests that the meridional P16 section might be better able to capture the density structure of the Pacific than the zonal P02 section. Extrapolation errors are estimated by comparing our estimates along P02 to our extrapolated estimates along P02 from P16 (Appendix A). For this calculation only, we use σ_θ instead of γ^N because γ^N is undefined in the northernmost Pacific using the calculation from Jackett and McDougall [1997]. The differences between these density coordinates are small for this extrapolation: for the region over which γ^N is defined, basin inventories extrapolated with σ_θ agreed with basin inventories estimates extrapolated using γ^N to within $0.3 \pm 1\%$.

Overall C_{anth} is estimated for both sections in the CLIVAR and GO-SHIP decades by adding the eMLR ΔC_{anth} estimates to the WOCE-era ΔC^* -based C_{anth} estimates by *Sabine et al.* [2002] in the GLODAPv1.1 bottle data

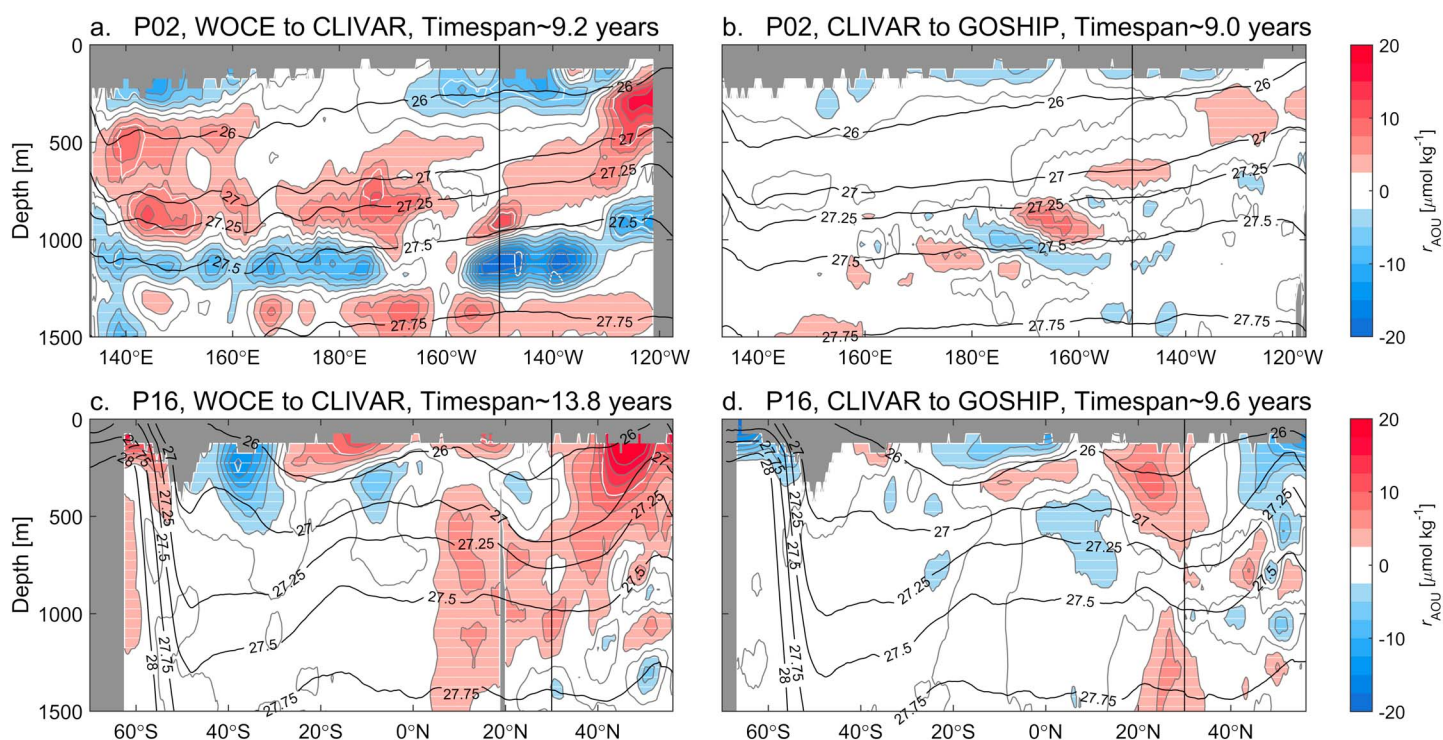


Figure 4. Sections of r_{AOU} (equation (6)) or the portions of r_{AOU} that are not removed by our eMLR method. Sections are (a) P02 (east-west at $\sim 30^\circ\text{N}$) in the earlier decade, (b) P02 in the recent decade, (c) P16 (north-south at $\sim 150^\circ\text{W}$) in the earlier decade, and (d) P16 in the recent decade. Thin white line hashing of changes indicates that the change is not statistically significant. Vertical black lines indicate crossovers between the two sections, and curved black lines indicate surfaces of constant γ^{N} . These estimates are only averaged for the five regressions that have r_{AOU} and do not include AOU as a predictor.

product [Key *et al.*, 2004]. These WOCE-era ΔC^* estimates are first interpolated in the γ^{N} space observed during the CLIVAR and GO-SHIP occupations. One or both ΔC_{anth} estimates are then added to update the overall C_{anth} estimates. Aragonite saturation state (Ω_{A}) and pH are calculated from the measured C_{T} and A_{T} , and the preindustrial Ω_{A} and pH (calculated from measured A_{T} and the difference between the measured C_{T} and estimated C_{anth}) are subtracted from them. These calculations provide an estimate of the overall impact of C_{anth} on Ω_{A} ($\Delta\Omega_{\text{A}}$) and pH (ΔpH). We linearly interpolate (and extrapolate where necessary) these estimates in time from 1991 to 2015. The overall C_{anth} estimates and a simple animation showing C_{anth} and $\Delta\Omega_{\text{A}}$ over time are provided as supporting information.

Errors are assessed in Appendix A. Uncertainty estimates should be considered to be $\pm 1\sigma$, though 95% confidence intervals are used for determining statistical significance. The error analysis reveals that eMLR C_{anth} estimates vary by $\pm 3.3 \mu\text{mol kg}^{-1} C_{\text{anth}}$ between regression coefficient sets. This uncertainty would apply in full to nonensemble eMLR estimates that rely on a single property combination and would be the largest single component of estimate uncertainty for such estimates. However, we argue (and show in Appendix B) that this error is reduced for our 16-member ensemble eMLR. The largest remaining source of uncertainty for this analysis is then potential errors in C_{T} measurements or the adjustments applied to them.

3. Results and Discussion

Results are presented from the surface to 1500 m depth. We do not find any statistically significant changes below this depth in the Pacific. This is expected because of the great age of most deep Pacific waters [Matsumoto, 2007; Gebbie and Huybers, 2012]. While changes in Antarctic Bottom Water C_{anth} are possible, we do not expect these changes to be detectable on decadal timescales using our methods.

3.1. r_{AOU}

We briefly examine r_{AOU} averaged for the five regressions (see Table 2) that did not use AOU as a regression parameter (Figure 4). These r_{AOU} estimates are not comprehensive estimates of ΔAOU in a water mass

because the eMLR regressions with N and Si remove the portions of ΔAOU that correlate with these nutrients, as recently pointed out by *Chu et al.* [2016]. It is therefore likely that most AOU changes from shifts in net organic matter decomposition—resulting from rain rate changes or circulation shifts—are missing from r_{AOU} estimates. We attribute the remaining r_{AOU} signal primarily to variations in organic matter export that occur near the surface and are followed by reequilibration of O_2 and C_T (but not nutrients) with the atmosphere. Phrased differently, we believe that the r_{AOU} term primarily reflects variations in *Broecker's* [1974] quasi conservative tracer “NO,” which is oxygen adjusted for the amount of nitrate present. Since CO_2 and O_2 can both be restored to equilibrium by gas exchange, the AOU adjustment (equation (8)) remains appropriate for eMLR analyses when AOU is not used as a regression parameter.

Along both sections, our r_{AOU} estimates for the first decade (Figures 4a and 4c) have a similar pattern, though of generally smaller magnitude, to the estimates obtained for the same decade by *Sabine et al.* [2008]. An exception is found for waters shallower than 400 m depth along P02, where *Sabine et al.* [2008] find consistently positive r_{AOU} and we do not. In this region their results appear dissimilar from our mean estimates but still fall within the range of results from individual regression coefficient combinations. This apparent disagreement highlights how sensitive r_{AOU} patterns are to the choice of regression coefficients (Appendix A). Due in part to this sensitivity, most of the mean r_{AOU} estimates cannot be distinguished from 0 at >95% confidence. Another likely reason for the predominance of nonsignificant r_{AOU} estimates is that the majority of ΔAOU is correlated with nutrient changes and removed by our eMLR procedure, and therefore, the mean r_{AOU} estimates are small. While mostly small, significant positive r_{AOU} estimates are found near the northern and eastern edges of the P16 and P02 sections, respectively, in water between 26 and 27 $kg\ m^{-3}\ \gamma^N$ extending between the base of the mixed layer and ~500 m. Another exception is a broadly distributed, but rarely statistically significant, positive r_{AOU} between 27 and 27.25 $kg\ m^{-3}$ across P02 during the earlier decade. *Emerson et al.* [2004], *Deutsch et al.* [2006], and *Mecking et al.* [2008] attributed similar but significantly more intense changes in modeled and observed AOU along density surfaces to a decrease in ventilation of the deepest and densest (26.6 $kg\ m^{-3}\ \sigma_\theta$ or about 26.7 $kg\ m^{-3}\ \gamma^N$) portions of the North Pacific Subtropical Gyre. A more direct comparison to their ΔAOU estimates can be made with “ r_{AOU} ” estimates obtained using only θ and S (not shown), which were broadly 10 to 20 $\mu mol\ kg^{-1}$ higher than our mean ensemble eMLR r_{AOU} estimates between the 26 and 27 $kg\ m^{-3}\ \gamma^N$ surfaces along P02 and the northernmost portions of P16. These estimates from only θ and S , which we contend only have ΔAOU from shifts in the distributions of water masses removed, more closely match *Mecking et al.'s* [2008] findings. The band of negative r_{AOU} estimates found near and below the 27.5 $kg\ m^{-3}$ isoneutral surface along P02 is not present when the regression windows are doubled in size (section 2.2). These estimates are therefore likely artifacts from how few measurement sets were used in the regressions over this depth range for the WOCE P02 section.

Our r_{AOU} estimates are of smaller magnitude along both sections for the recent decade (Figures 4b and 4d) than for the earlier decade. However, in the recent decade, r_{AOU} estimates obtained using only θ and S (not shown) were again large and positive between 25.5 and 26.7 $kg\ m^{-3}\ \gamma^N$ between ~160°E and 160°W along P02 but negative east of ~140°W at densities lighter than 26 $kg\ m^{-3}\ \gamma^N$. This observation suggests that waters perhaps continued to age between ~160°E and 160°W while being partially ventilated in the shallowest and easternmost portions of the gyre (cf. Figures 5a and 5b).

3.2. ΔC_{anth}

Estimates of ΔC_{anth} along the two sections for both decades (Figure 5) reveal a familiar pattern of ΔC_{anth} of 8–13 $\mu mol\ kg^{-1}$ near the surface extending to depth in the lower density thermocline waters of the subtropical gyres. The surface change is slightly larger in the subtropics where higher temperatures and alkalinities lead to greater CO_2 storage for a given pCO_2 change. In the interior, C_{anth} penetration is deeper in the Southern Pacific (>5 $\mu mol\ kg^{-1}$ to at least 700 m depth in both decades) where Subantarctic Mode Water (SAMW) and Antarctic Intermediate Water (AAIW) ventilate the deepest portions of the subtropical thermoclines. The less voluminous mode and intermediate water masses of the North Pacific Gyre thermocline create a shallower local ΔC_{anth} maximum in the Northern Hemisphere. Penetration is shallowest in the subpolar, subantarctic, equatorial, and eastern boundary current regions where older waters upwell that have not been as recently exposed to the atmosphere. Along P02, ΔC_{anth} broadly tracks isopycnal surfaces that shoal rapidly west of 140°E across the northward flowing Kuroshio and gradually east of there across the generally

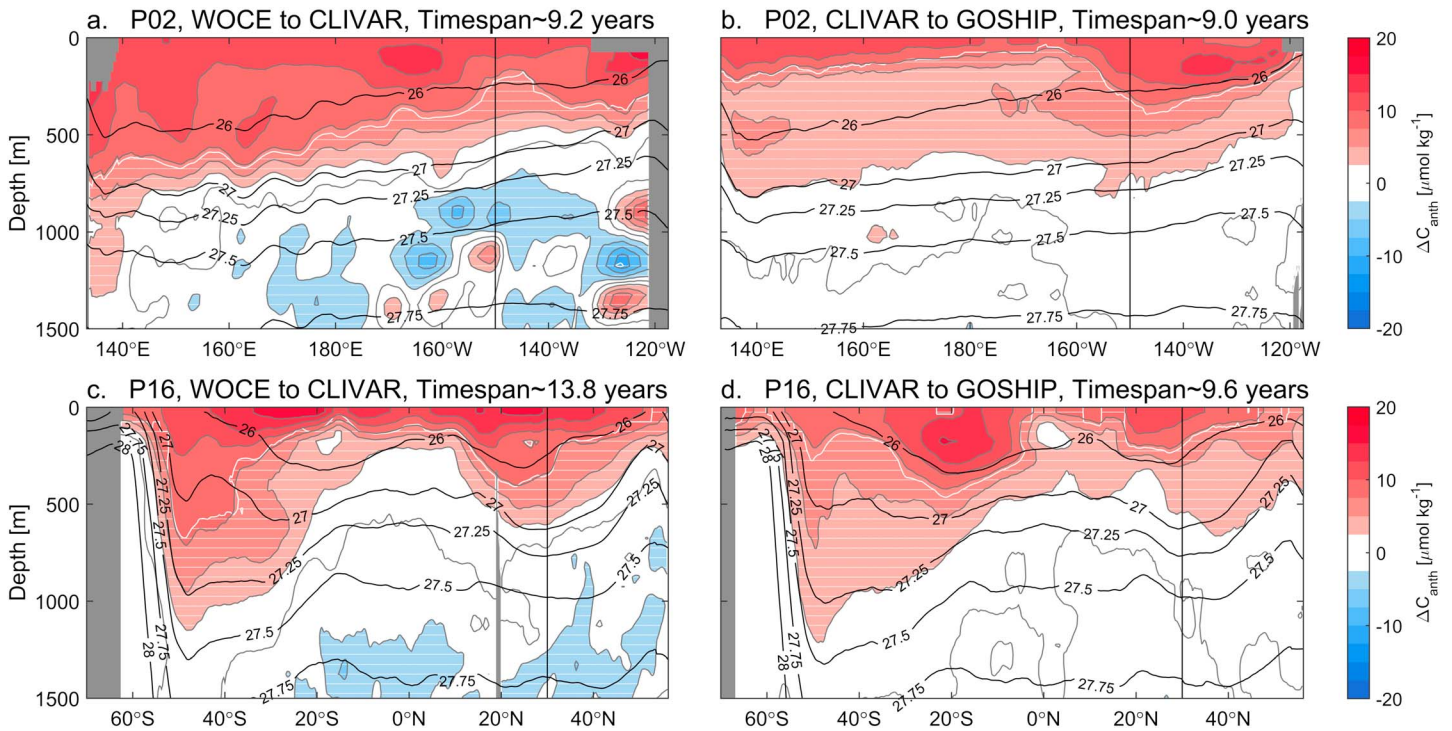


Figure 5. Sections of ΔC_{anth} (equation (8)) or estimates of the decadal increases in C_{anth} along each section. Sections are (a) P02 (east-west at $\sim 30^\circ\text{N}$) in the earlier decade, (b) P02 in the recent decade, (c) P16 (north-south at $\sim 150^\circ\text{W}$) in the earlier decade, and (d) P16 in the recent decade. Thin white line hashing of changes indicates that the change is not statistically significant. Vertical black lines indicate crossovers between the two sections, and curved black lines indicate surfaces of constant γ_N .

southward flowing gyre. An exception is found east of 160°W along P02 in the recent decade where there is a local ΔC_{anth} maximum. This exception suggests that there has been an increase in ventilation along the eastern portion of P02 during the recent decade, as suggested earlier in section 3.1 and as found along the P17N section (also in the NE Pacific) by *Chu et al.* [2016]. ΔC_{anth} extends across the thermocline and is found in North Pacific Intermediate Water [Talley, 1993; Yasuda, 1997] and multiple varieties of North Pacific mode water [Hanawa and Talley, 2001].

The ΔC_{anth} distributions agree with those found by *Sabine et al.* [2008] for the earlier decade within expected uncertainties. We find smaller C_{anth} increases in the triangle bound by (0°S at 200 m, 25°S at 200 m, and 25°S at 800 m) depth, though *Sabine et al.* [2008] also find a minimum at 20°S at ~ 200 m depth. Along P02, we both find local maxima near the California and Kuroshio Currents, though our Kuroshio ΔC_{anth} maximum is less pronounced than theirs. We also find higher ΔC_{anth} at the surface across P02 than they do. Disagreements between our estimates and theirs of this order ($\sim 3\text{--}5 \mu\text{mol kg}^{-1}$, 1σ) are expected because, as *Plancherel et al.* [2013] showed and we show in Appendix A, the nonensemble eMLR estimate distributions provided by other eMLR studies are highly sensitive to the choice of regression parameters.

Comparing ΔC_{anth} estimates for the earlier and recent decades reveals several changes in ΔC_{anth} estimate patterns. To quantify these shifts, we normalize the ΔC_{anth} distributions to a 10 year time span and then directly difference them ($\Delta\Delta C_{\text{anth}}$, for a change in the change, in Figure 6). The largest statistically significant feature is a large increase in ΔC_{anth} in densities between the 26 kg m^{-3} isoneutral surface and the base of the mixed layers between 30°S and 10°S along P16. A second broad ΔC_{anth} decrease can be seen along P02 in densities lighter than 26 kg m^{-3} γ_N west of 160°W (and somewhat deeper farther west). While these ΔC_{anth} changes along P02 are rarely statistically significant individually, they are collectively a distinguishable feature. In sections 3.3 and 3.5, we rule out the possibility that either of these changes result from shifts in the locations of water masses, so we attribute them instead to changes in the degree of ventilation of water masses at these locations. A likely explanation for the South Pacific storage change increase is variability in the overturning of the Southern Pacific Subtropical Cell (STC), which transports water equatorward along

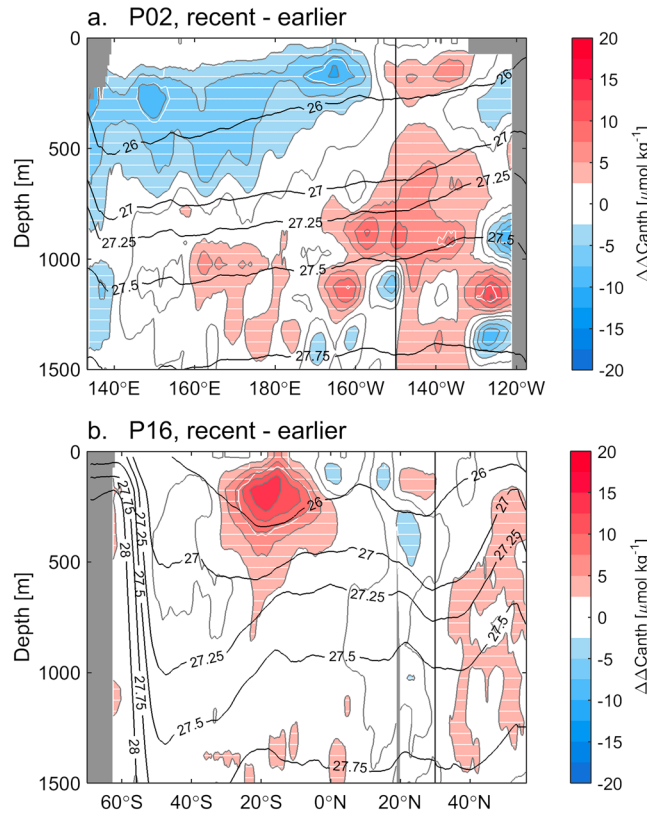


Figure 6. Differences between decadal uptake of C_{anth} in the recent and earlier decades considered ($\Delta\Delta C_{anth}$). These estimates are calculated directly along (a) P02 (east-west at $\sim 30^\circ N$) and (b) P16 (north-south at $\sim 150^\circ W$). Thin white hashing of changes indicates that the change is not statistically significant. Vertical black lines indicate crossovers between the two sections, and curved black lines indicate surfaces of constant γ^N .

measured in shifting water masses (i.e., P in equation (2)). For example, a passing eddy during a hydrographic occupation would rearrange the density structure of the water being measured and result in a redistribution of the physical and biogeochemical measurements used in equations (5) and (6). We estimate the impact of this variability on ΔC_{anth} estimates as the differences between estimates obtained from different property distributions (i.e., using P from a different decade). Expressed in the notation of equation (2), we estimate this term as follows:

$$\text{"Variability" } \Delta C_{anth} = f_2(P_2) - f_1(P_2) - (f_2(P_1) - f_1(P_1)) \quad (9)$$

for a WOCE to CLIVAR comparison. This "Variability" ΔC_{anth} estimate averages (mean \pm RMS) $0.1 \pm 0.9 \mu\text{mol kg}^{-1}$ between the base of the mixed layer and 1500 m depth in our four sets of estimates, suggesting that it is a small contribution to overall ΔC_{anth} estimate variability. However, eMLR can fail to identify local ΔC_{anth} variability when determining regression coefficients with measurements made over broad areas. Therefore, this analysis does not rule out such variability meaningfully redistributing C_{anth} ; it merely suggests a small role for such variability in governing eMLR ΔC_{anth} estimates.

3.4. Column Inventory Change Rates

As shown in section 3.2, ΔC_{anth} is greatest in low-density recently ventilated thermocline waters. C_{anth} column inventory increases (Figure 7) are therefore greatest along P02 in the earlier decade in the Eastern Pacific where isopycnal surfaces are deepest. A similar pattern is seen along P02 in the recent decade though the region of elevated increases east of $160^\circ W$ noted in section 3.2 is also apparent. Mean column inventory stayed approximately constant at 0.53 ± 0.11 and $0.46 \pm 0.11 \text{ mol C m}^{-2} \text{ a}^{-1}$ along P02 in the earlier and

the $\sim 25 \text{ kg m}^{-3} \gamma^N$ isoneutral surface, where the anthropogenic carbon transport of this feature is at a maximum [Nakano et al., 2015]. The STC exhibits substantial decadal variability and was declining prior to 1998 [McPhaden and Zhang, 2002] before rebounding [McPhaden and Zhang, 2004] and intensifying through the recent decade [England et al., 2014]. The (barely statistically significant) portions of this signal in waters denser than $26 \text{ kg m}^{-3} \gamma^N$ may be due to an intensification of SAMW formation in the earlier decade [Waugh et al., 2013] that, sustained in the recent decade, is now propagating farther North.

3.3. ΔC_{anth} Variability

While eMLR removes the effects of many forms of subdecadal variability on C_T , the method does not also remove all subdecadal variability in C_{anth} . For example, Woosley et al. [2016] used eMLR to show mesoscale eddies redistribute C_{anth} along sections. Water mass redistributions such as eddies and frontal shifts can appear in ΔC_{anth} estimates when the eMLR regressions are applied to property distributions that were measured

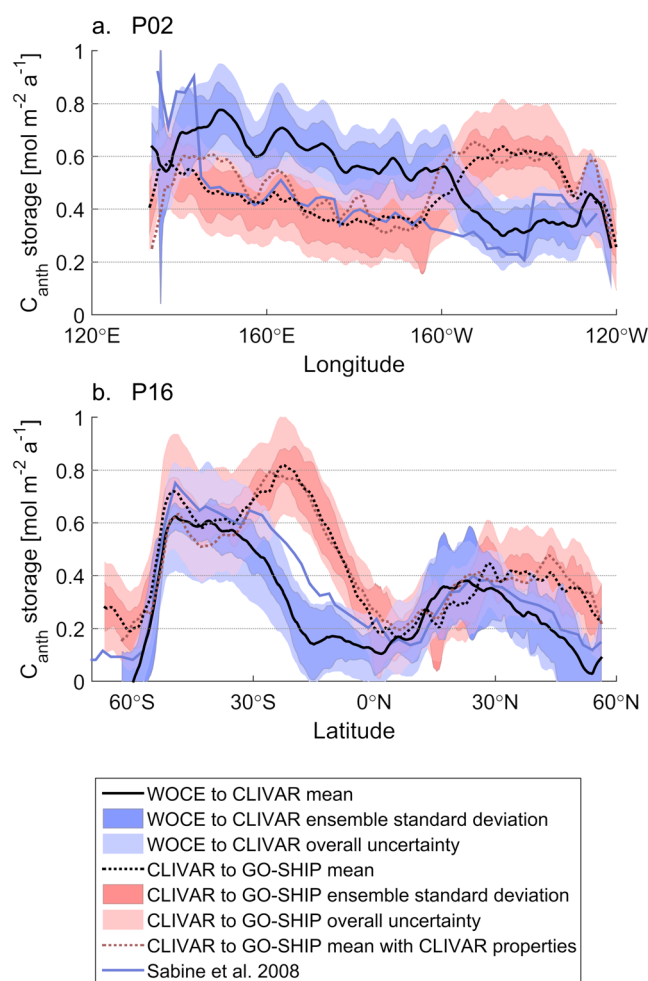


Figure 7. Column C_{anth} inventory changes. (a) P02 (east-west at $\sim 30^\circ\text{N}$) and (b) P16 (north-south at $\sim 150^\circ\text{W}$). Light blue and red shading around black lines (ensemble means) indicate the overall uncertainties on our estimates. Dark blue and red shading indicates the standard deviation between ensemble members. Solid blue lines are estimates from *Sabine et al.* [2008] for the same sections and earlier WOCE to CLIVAR decades. Orange dotted lines provided for comparison with the black lines are estimates of the column inventory change rates calculated using the CLIVAR era property distributions instead of the GO-SHIP era distributions. We argue that the differences between the orange and black dotted lines represent the effects of subdecadal redistribution of C_{anth} (section 3.3).

recent decades, respectively. Along P16 there is a double hump characteristic of the deeper penetration of low density mode and intermediate water types in the North and South Pacific Gyres than in the surrounding Antarctic, subpolar, and equatorial Pacific. A similar pattern is seen in the recent decade along P16, though a new local column storage maximum at $\sim 20^\circ\text{S}$ is also visible. Mean C_{anth} storage along P16 increased slightly from 0.29 ± 0.10 to $0.45 \pm 0.11 \text{ mol C m}^{-2} \text{ a}^{-1}$ in the earlier and recent decades, respectively. This change was driven by a statistically significant C_{anth} storage acceleration from 0.36 ± 0.10 to $0.58 \pm 0.10 \text{ mol C m}^{-2} \text{ a}^{-1}$ in the South Pacific and a comparable or increasing North Pacific storage of 0.23 ± 0.1 and $0.31 \pm 0.1 \text{ mol C m}^{-2} \text{ a}^{-1}$ in the earlier and recent decades, respectively.

The lighter blue bands in Figure 7 indicate the overall uncertainty estimates (1σ) for our eMLR method (see Appendix A). A major source of the overall uncertainty for traditional eMLR and ensemble eMLR is uncertainty in the C_T measurements or measurement adjustments (section 2.1), where a $1 \mu\text{mol kg}^{-1}$ error over 10 years—integrated over 1000 m of seawater—creates a $\sim 0.1 \text{ mol m}^{-2} \text{ a}^{-1}$ storage change error. With these large uncertainties, it is difficult to conclude whether shifts in column storage are real, especially because errors in adjustments derived from CLIVAR era measurements could have opposing effects on the two decadal records, amplifying the apparent differences. Nevertheless, the largest apparent change is more than double the overall uncertainty; at 15.75°S , the decadal column inventory increase grew from 0.15 to

Table 3. Pacific Decadal C_{anth} Storage for the Latitude Bands Spanned by P16 in Pg C decade^{-1} ^a

Latitude Band	WOCE to CLIVAR	CLIVAR to GO-SHIP
70 to 60°S	^b	0.65
60 to 50°S	0.56	0.84
50 to 40°S	0.90	0.97
40 to 30°S	0.96	1.07
30 to 20°S	0.65	1.31
20 to 10°S	0.35	1.20
10 to 0°S	0.29	0.72
0 to 10°N	0.46	0.56
10 to 20°N	0.79	0.52
20 to 30°N	0.60	0.64
30 to 40°N	0.35	0.53
40 to 50°N	0.13	0.35
50 to 60°N	0.07	0.21
Southern Hemisphere	3.8 ± 1.0	6.8 ± 1.7
Northern Hemisphere	2.4 ± 0.6	2.8 ± 0.7
Total (60°S to 60°N)	6.1 ± 1.6	8.9 ± 2.2

^aThe “total” values include estimates for (not shown) data-poor latitude bands from 60°N to 67°N and 70°S to 80°S and therefore do not exactly equal the sum of all rows.

^bInsufficient data.

$0.61 \text{ mol C m}^{-2} \text{ a}^{-1}$. The second largest changes are the increases noted along the eastern portion of P02. As discussed throughout section 3, we attribute these two features primarily to shifts in the degree of ventilation of these water masses.

The orange dotted lines in Figure 7 show column inventory estimates obtained from ΔC_{anth} estimates created from the property distributions of the CLIVAR decades instead of the GO-SHIP decades (see section 3.3). The broad similarity between the orange and black dotted lines on average reinforces the idea that shifts in the locations of water masses alone cannot account for the regional shifts in ventilation seen near 20°S along P16 or in the Eastern Pacific along P02. Shifts in

the degree of ventilation of water masses are therefore a more likely explanation. The differences between the orange and black dotted lines show the effects of decadal and shorter-term variability on the C_{anth} distributions (e.g., eddies and frontal shifts).

Our estimates from the earlier decade generally match estimates in the literature to within uncertainties. *Sabine et al.* [2008] estimated column inventories with eMLR along both of these sections, so we plot their results directly with ours (solid blue lines in Figure 7). Considering P02 and P16 results collectively, their results and ours agree to within uncertainties (i.e., the blue lines are within the light blue windows for >68% of the two panels). *Kouketsu et al.* [2013] used the ΔnC_T^{CAL} method—which uses a collection of assumptions in lieu of empirical relationships to adjust for the influences of natural variability—to estimate anthropogenic carbon changes between the 1990s and 2000s along a number of sections in the Pacific. They found a similar (within $\pm 1\sigma$) column inventory change pattern in the southern portion of P16, with high $\sim 0.6 \pm 0.1 \text{ mol C m}^{-2} \text{ a}^{-1}$ storages south of 30°S that drop to 0.1 ± 0.1 by 15°S. Their Northern Hemisphere storage estimates are comparable to ours along P02 and P16 also, excepting between 20°N and 30°N where they find $0.9 \pm 0.1 \text{ mol C m}^{-2} \text{ a}^{-1}$ storage. *Williams et al.* [2015] also used eMLR to estimate column inventories along S4P in the Pacific sector of the Southern Ocean (67°S) over the period spanning both of the decades considered and found an average of $0.1 \text{ mol C m}^{-2} \text{ a}^{-1}$. Our nearest estimates along P16 that span both decades (at 62.5°S) average $0.06 \pm 0.1 \text{ C m}^{-2} \text{ a}^{-1}$. *Murata et al.* [2007] used ΔnC_T^{CAL} to estimate column C_{anth} inventories along P06, which crosses P16 at 32°S and spans a similar time period to our earlier decade. They find a C_{anth} storage of $0.64 \pm \sim 0.4 \text{ mol C m}^{-2} \text{ a}^{-1}$ west of P16 and $1.25 \pm \sim 0.4 \text{ C mol m}^{-2} \text{ a}^{-1}$ east of P16. Our estimate of $0.53 \pm 0.11 \text{ mol C m}^{-2} \text{ a}^{-1}$ is within uncertainties of one of these estimates and is lower than the other. *Chu et al.* [2016] estimate C_{anth} changes along P17N between 2001 and 2012. The P17N section angles from near P16 at $\sim 50^\circ\text{N}$ to near P02 at 135°W . *Chu et al.*'s [2016] estimates decrease from $0.55 \pm 0.12 \text{ mol m}^{-2} \text{ a}^{-1}$ at 34°N to $\sim 0.2 \pm 0.12 \text{ m}^{-2} \text{ a}^{-1}$ at 50°N , while the nearest estimates on our sections in the recent decades are $0.50 \pm 0.11 \text{ mol m}^{-2} \text{ yr}^{-1}$ and $0.35 \pm 0.11 \text{ mol m}^{-2} \text{ yr}^{-1}$, respectively. They attribute differences between their estimates and the estimates of *Sabine et al.* [2008] along P16 and P02 to differences in methods used and regions considered. Our results confirm the importance of such methodological differences and also suggest that differences in the timeframes considered are also likely important.

3.5. Basin Inventory Changes

Basin inventory change estimates are averaged by 10° latitude bands and by hemispheres in Table 3. Pacific C_{anth} storage increased on average from 6.1 ± 1.6 to $8.9 \pm 2.2 \text{ Pg C decade}^{-1}$. By comparison, *Woosley et al.* [2016] found that anthropogenic carbon storage also increased in the recent decade in the North Atlantic,

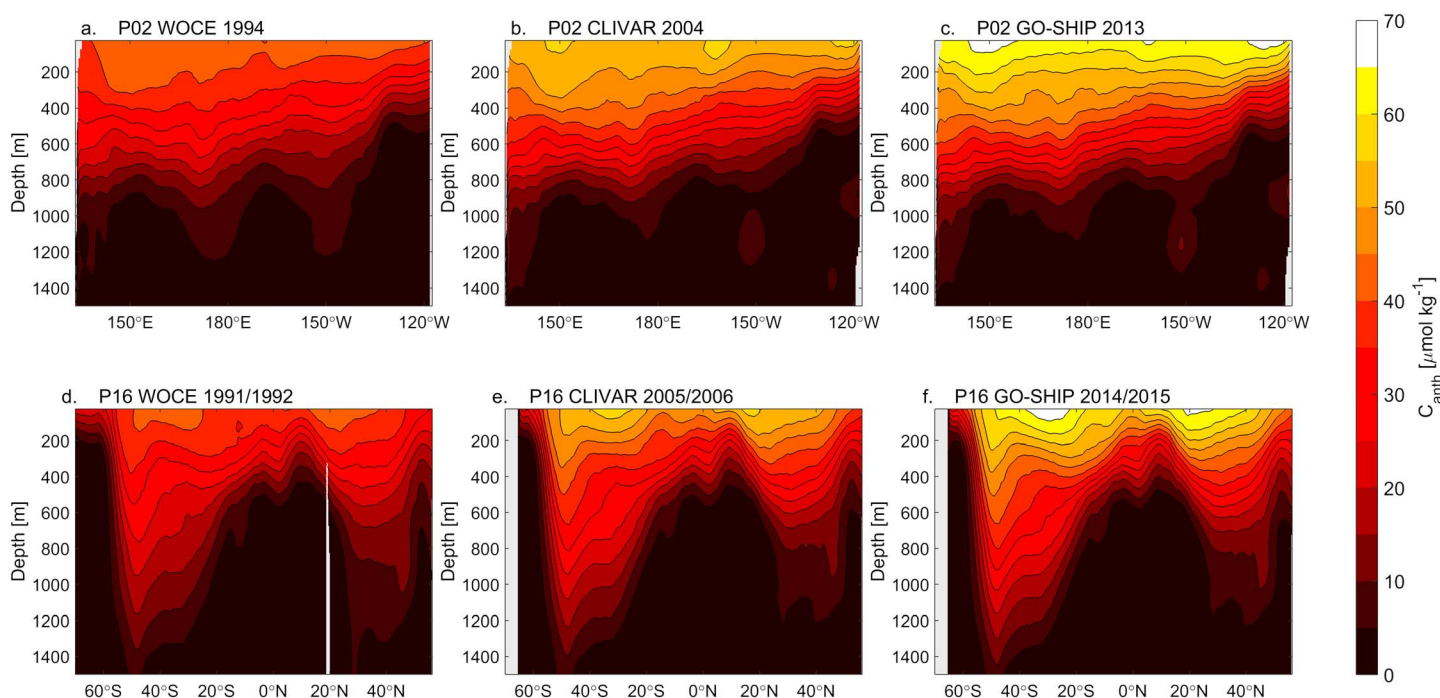


Figure 8. Estimates of total C_{anth} accumulation since the Preindustrial Era. Sections are (a) P02 (east-west at $\sim 30^\circ\text{N}$) in the WOCE occupation, (b) P02 in the CLIVAR occupation, (c) P02 in the GO-SHIP occupation, (d) P16 (north-south at $\sim 150^\circ\text{W}$) in the WOCE occupation, (e) P16 in the CLIVAR occupation, and (f) P16 in the GO-SHIP occupation.

leading to an overall Atlantic storage increase from 5.1 to $8.1 \text{ PgC decade}^{-1}$. Pacific storage is comparable to Atlantic storage—despite the formation of North Atlantic Deep Water in the Atlantic—because of the larger volume of the Pacific Ocean. The Pacific storage increase between the earlier and the later decades was primarily driven by a large increase in Southern Pacific storage from 3.8 ± 1.0 to $6.8 \pm 1.7 \text{ PgC decade}^{-1}$. The North Pacific inventory increase remained constant to within uncertainties at $2.4 \pm 0.6 \text{ PgC decade}^{-1}$ in the earlier and $2.8 \pm 0.6 \text{ PgC decade}^{-1}$ in the later decade. Pacific decadal storage increases outpaced the slightly increased rate of atmospheric CO_2 accumulation. The increases in Southern Pacific storage estimates cannot be explained by variability in the depths of isopycnal surfaces because both of these estimates were extrapolated onto the same World Ocean Atlas climatological density field. This suggests that changes in ventilation, or displacement of water masses with differing degrees of ventilation, also occurred. We note that our decadal basin and latitude band inventory estimates might be overestimates if any shifts were unique to the time or longitude windows around the GO-SHIP P16 occupation (e.g., related to El Niño or the Blob) [Amaya *et al.*, 2016]. Upcoming reoccupations of the P15 (170°W), P06 ($\sim 30^\circ\text{S}$), and P18 (103°W) lines will afford the opportunity to test temporal and regional extent of these changes and will provide means to reduce the uncertainties associated with these extrapolations from only a single section. There are reoccupied sections that could be analyzed in the Northern Pacific as well, including P14 (180°E).

3.6. Overall C_{anth} and Impacts on pH and Aragonite Saturation

C_{anth} distributions have been steadily increasing throughout the gyre thermoclines of the Pacific (Figure 8). The highest concentrations of 65 to $70 \mu\text{mol kg}^{-1}$ C_{anth} are found in the surface ocean in the GO-SHIP occupations, corresponding the approximate expected increase from equilibration with a changing atmosphere (assuming seawater at $\sim 20^\circ\text{C}$ with a salinity of 33, an A_T 2200, and a $p\text{CO}_2$ increase from 280 to 400 ppm). Surface concentrations fall at higher latitudes where colder seawater temperatures correspond to less C_{anth} gain for a given atmospheric change. C_{anth} concentrations fall also with depth. In the interior, C_{anth} becomes a passive tracer, and distributions broadly track the isopycnal surfaces along which advection and diffusion are strongest. Upwelling lifts isopycnal surfaces, decreasing C_{anth} along, for example, equatorial latitudes and the U.S. West Coast.

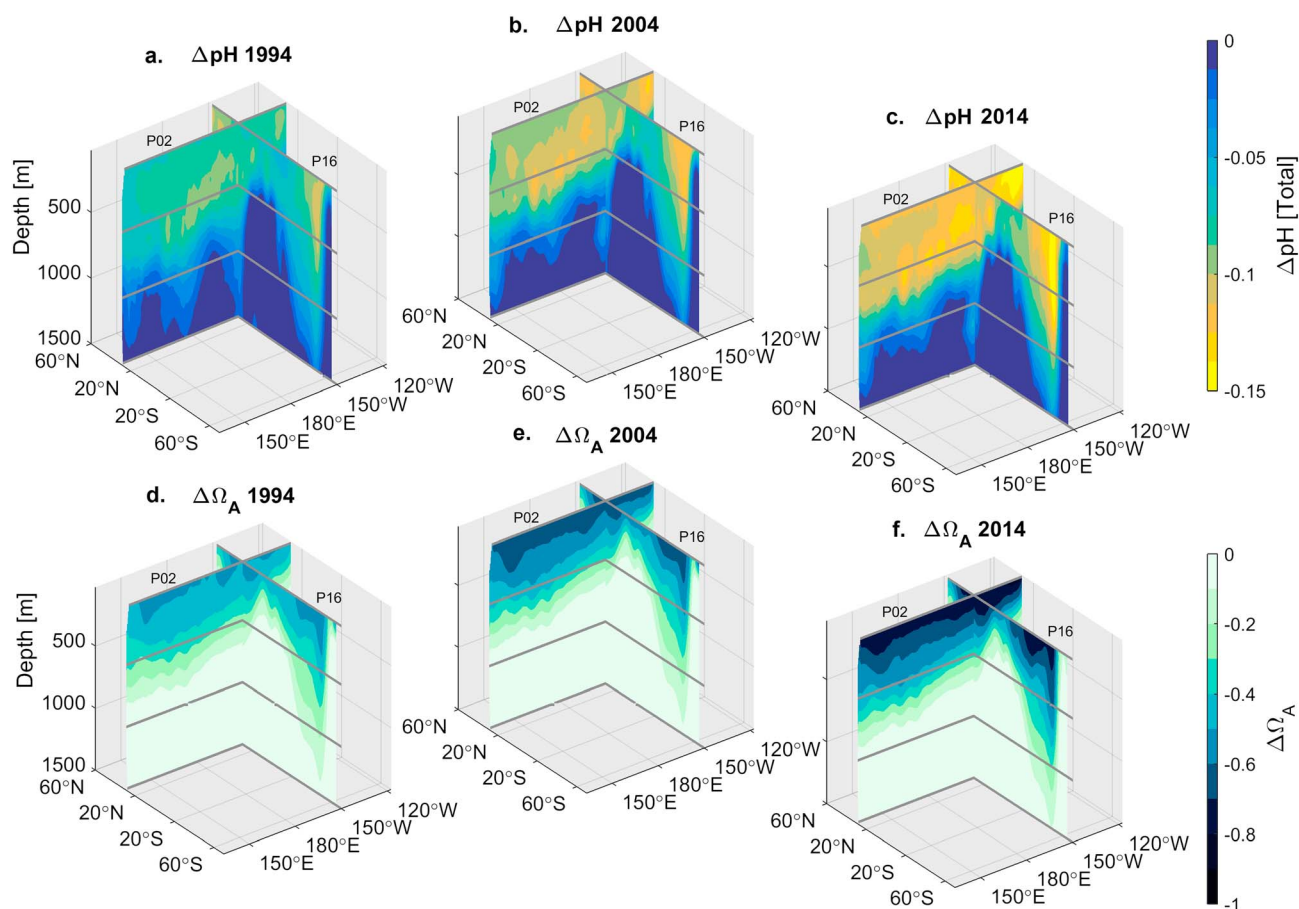


Figure 9. The 3-D sections of the net impact of ocean acidification on (a–c) pH (total scale) and (d–f) aragonite saturation ($\Delta\Omega_A$) along P02 (sections from lower left to upper right) and P16 (sections from upper left to lower right) from the Preindustrial Era to (Figures 9a and 9e) 1994, (Figures 9b and 9d) 2004, and (Figures 9c and 9f) 2014.

As expected [Doney *et al.*, 2009; Feely *et al.*, 2009, 2012], C_{anth} storage has continued to acidify the ocean and decrease carbonate mineral saturations. Aragonite saturation decreases from C_{anth} storage increased in approximate proportion to the C_{anth} concentrations stored since the Preindustrial Era ($\Delta\Omega_A$ in Figures 9d–9f), while changes in pH were more complex (ΔpH in Figures 9a–9c). Net surface $\Delta\Omega_A$ ranged between -0.41 and -0.57 in 1994 and between -0.57 and -0.82 in 2014 (Table 4), while surface ΔpH ranged from -0.06 to -0.10 in 1994 and from -0.08 to -0.14 in 2014. Surface aragonite saturation (and pH) fell at an average rate of 0.29% (0.020%) per year and 0.34% (0.023%) per year in the earlier and recent decades, respectively. The acceleration of these surface acidification signals is due to accelerating atmospheric CO_2 concentration increases.

Understanding pH and Ω_A change variability with latitude (along P16 in Table 4) and with depth (Figure 9) requires understanding two properties of the carbonate system in seawater: First, colder seawater holds more C_T at a given $p\text{CO}_2$ or pH and has lower Ω_A . Second, the higher the C_T of seawater, the less a given change in $p\text{CO}_2$ will change C_T and Ω_A . High-latitude surface waters that are naturally rich in C_T due to cold temperatures (e.g., polar surface seawater) exhibit smaller changes in Ω_A . Similarly, upwelling regions (e.g., equatorial surface seawater) also exhibit a smaller Ω_A decreases for fixed $p\text{CO}_2$ changes than warm low- C_T surface waters (e.g., subtropical surface waters). This accounts for the two Ω_A change maxima at midlatitudes in Table 4. The sensitivity of pH to a changing atmospheric $p\text{CO}_2$ increases as temperature decreases, whereas the opposite is true for Ω_A . For this reason, the magnitude of ΔpH reaches local maxima rather than local minima in cold high-latitude waters. Anthropogenic changes in pH are amplified at depth where pH is naturally lower—implying a larger change in $p\text{CO}_2$ and pH for a given change in C_T —and where there is no contact with the atmosphere to hold $p\text{CO}_2$ near the atmospheric value. For this reason, the largest pH

Table 4. Net Impacts of Ocean Acidification Since the Preindustrial Era on Surface Aragonite Mineral Saturation ($\Delta\Omega_A$) and pH (ΔpH) Estimated for Latitude Bands Along P16 (Running North-South at $\sim 150^\circ\text{W}$) in 1994, 2004, and 2014^a

Latitude Band	$\Delta\Omega_A$ 1994	$\Delta\Omega_A$ 2004	$\Delta\Omega_A$ 2014	ΔpH 1994	ΔpH 2004	ΔpH 2014
60 to 50°S	−0.29	−0.32	−0.39	−0.09	−0.10	−0.13
50 to 40°S	−0.56	−0.67	−0.78	−0.10	−0.12	−0.14
40 to 30°S	−0.57	−0.69	−0.82	−0.08	−0.10	−0.12
30 to 20°S	−0.52	−0.65	−0.79	−0.07	−0.09	−0.11
20 to 10°S	−0.44	−0.54	−0.70	−0.06	−0.07	−0.09
10 to 0°S	−0.44	−0.51	−0.60	−0.06	−0.07	−0.08
0 to 10°N	−0.47	−0.54	−0.63	−0.07	−0.08	−0.09
10 to 20°N	−0.52	−0.63	−0.74	−0.07	−0.09	−0.10
20 to 30°N	−0.54	−0.67	−0.80	−0.07	−0.09	−0.11
30 to 40°N	−0.55	−0.65	−0.77	−0.08	−0.10	−0.12
40 to 50°N	−0.49	−0.59	−0.69	−0.09	−0.11	−0.13
50 to 60°N	−0.41	−0.50	−0.57	−0.09	−0.12	−0.14
Average of all latitudes	−0.48	−0.58	−0.69	−0.08	−0.09	−0.11

^aUncertainties on these estimates are small (5–10%), but we do not account for unknown potential errors in our presumption of fixed average surface atmospheric disequilibrium since the WOCE occupation.

decreases are at ~ 500 m depth (Figure 9) where high near-surface C_{anth} storages combine with elevated subsurface C_T from biological remineralization. The large variability of the ΔpH signal can be attributed to the strong sensitivity of ΔpH to the naturally variable C_T distribution (cf. Figure 2). There is no comparable amplification for $\Delta\Omega_A$, which exhibits more laterally homogenous distributions (Figure 9).

4. Conclusions

We have used a modified eMLR method to estimate two decades of anthropogenic carbon storage along the P02 (east-west at $\sim 30^\circ\text{N}$) and P16 (north-south at $\sim 150^\circ\text{W}$) sections. C_{anth} storage increased in the Pacific Ocean from 6.1 ± 1.5 to 8.9 ± 2.2 PgC decade^{−1} between 60°N and 60°S , due largely to storage increases in the Southern Pacific. The increase in the rate of storage in the South Pacific is attributed to increased ventilation of the Pacific Subtropical Cell. Decadal storage was smaller west of 160°W along P02 in the recent decade and slightly higher east of there. This may be due to continued changes in the ventilation of the North Pacific Gyre thermocline. This hypothesis could be tested by examining changes in chlorofluorocarbon distributions and AOU. By 2014, C_{anth} storage had changed Pacific surface Ω_A and pH by an average of -0.69 and -0.11 , respectively.

We adapted the eMLR method to quantify and reduce the impact on our estimates of several semiarbitrary methodological choices. The primary modification is to use an ensemble of regression coefficients instead of a single set. We have tested our modified methods using model outputs with known values and found that each modification yields improved estimates. We also demonstrate the value of our ensemble approach for estimating a subset of uncertainties inherent to the eMLR method. Finally, we have demonstrated that our methods return similar estimates to within expected uncertainties to estimates from eMLR given in literature.

One weakness of our study is the need to extrapolate across the Pacific Ocean from just two sections in order to infer basin inventory changes. A greatly improved estimate of Pacific basin inventories will be possible following the completion of, for example, the P18, P15, and P06 lines planned for 2016 and 2017. Estimates of C_{anth} changes along these lines would also provide means to assess the spatial and temporal extent of the C_{anth} storage patterns observed.

Appendix A: Error Assessment

A common approach for estimating eMLR errors relies on propagation of residuals between regression estimates and measurements. We avoid this approach because unresolved modes of variability are not necessarily a problem for the eMLR method if the impact of the variability on C_T is constant between reoccupations [Goodkin *et al.*, 2011] or adjusted for using a ΔC_{bio} correction. Additionally, our use of multiple combinations of regression parameters revealed that regressions with relatively poor fits to data (e.g., Regression 2, lacking

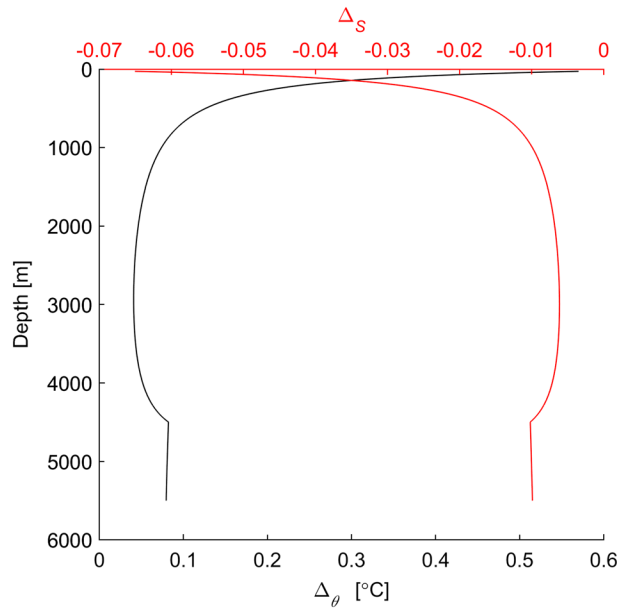


Figure A1. Example warming and freshening estimates for temperature (ΔT , black line, lower X axis) and salinity (ΔS , red line, upper X axis) as a function of depth for data from cruises 10 years apart. Equations for these lines are given in equations (A1) and (A2).

made with perturbed data. We perturb the later data sets of each data set pair by subtracting offsets that represent either long-term trends or measurement inaccuracies in the properties. For θ , S , C_T , AOU, N , and S_i , our perturbations (0.002, 0.002, 2, 2, 0.4, and $0.4 \mu\text{mol kg}^{-1}$, respectively) primarily reflect assumed measurement or adjustment uncertainties. For T and S , seasonal cycling and ongoing climate changes are creating greater property differences than measurement inaccuracies are. We therefore scale warming and freshening rate estimates for SAMW and AAIW from *Böning et al.* [2008] and for bottom waters from *Purkey and Johnson* [2010, 2013] with depth (z) and the length of time elapsed between occupations (δt), and add them together to obtain an ad hoc estimate of likely T and S changes (ΔS)

$$\Delta T = \left(0.009 \frac{600 \text{ m}}{z + 100 \text{ m}} + 0.005 \min \left(1, \frac{500 \text{ m}}{\text{abs}(z - 5000 \text{ m})} \right) \right) \frac{^\circ\text{C}}{\text{yr}} \delta t \quad (\text{A1})$$

$$\Delta S = \left(0.001 \frac{600 \text{ m}}{z + 100 \text{ m}} + 0.0005 \min \left(1, \frac{500 \text{ m}}{\text{abs}(z - 5000 \text{ m})} \right) \right) \frac{1}{\text{yr}} \delta t \quad (\text{A2})$$

The first terms in parentheses reflect changes in thermocline water masses. The second terms use minimum functions to allow AABW changes to apply uniformly over the 4500 to 5500 m depth range and decrease outside of this range. Figure A1 is an example of the changes that would be assigned T and S from sections repeated 10 years apart. The six perturbed data sets are then propagated through our calculations (omitting the deep data difference adjustment), and the differences between the estimates produced with the perturbed and unperturbed runs are used as error estimates. Differences between the six perturbed runs and the unperturbed run create six sets of C_{anth} concentration, column inventory, and basin inventory error estimates (e_1 to e_6). For column and basin inventory estimates, e_1 and e_2 —representing uncertainties in C_T and AOU—are divided by two because we are more confident in our data set adjustments than in individual measurements for these measurements. These perturbations only affect our estimate uncertainties, so errors in our assumed rates of warming and freshening have no impact on our C_{anth} estimates.

Plancherel et al. [2013] showed that eMLR estimates are sensitive to the choice of properties included in the regressions. We estimate the resulting uncertainty as the standard deviation of the population of C_{anth} , column inventory, and basin storage estimates from the 16 regression property combinations (S_{16}). This uncertainty only reflects errors in our estimate of an ideal mean ensemble eMLR estimate and does not

both AOU and N) produce ΔC_{anth} estimates that agree within expectations with estimates for regressions with better fits.

Instead, we build our error estimate from a consideration of the likely error sources as follows: (1) measurement errors or errors in our measurement adjustments (see section 2.1), (2) violations of the eMLR assumption that C_T changes from C_{anth} increases are the only nonstationary mode of variability, (3) the semiarbitrary choice of regression constant combinations, and (4) and other deficiencies inherent on eMLR.

Errors from these sources are estimated independently and combined as the square root of the sum of squared error contributions from these four items.

Errors from the first two sources are estimated using C_{anth} estimates

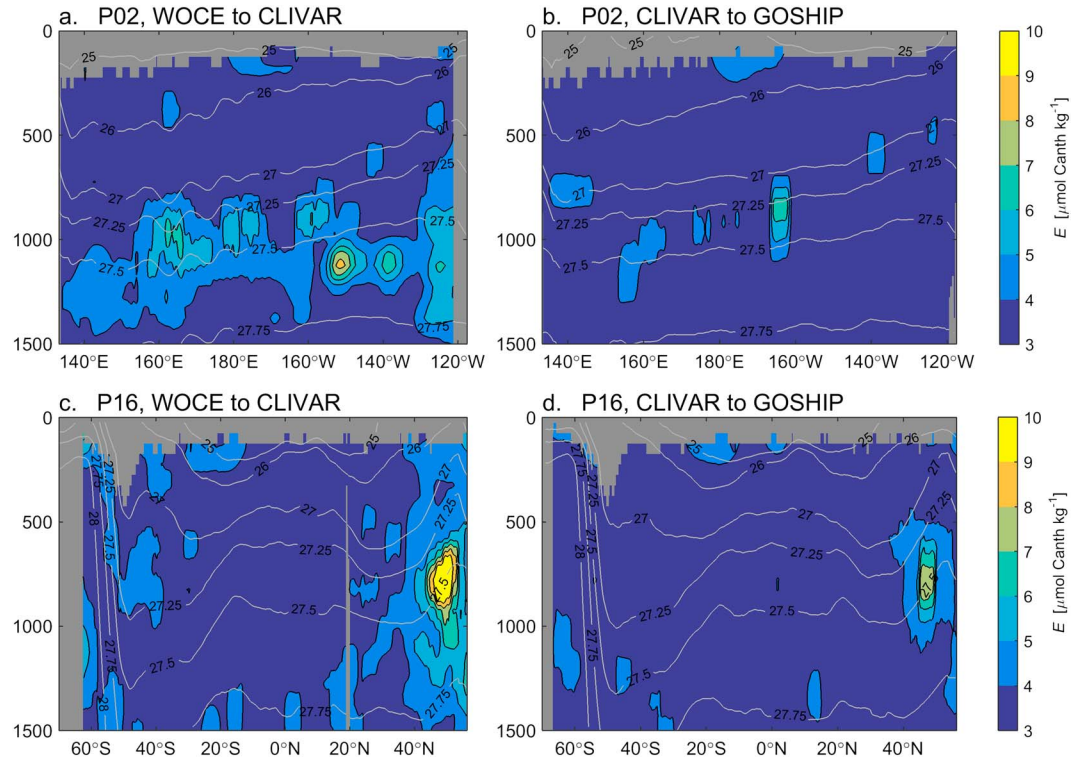


Figure A2. Sections of regionally varying overall uncertainty estimates E . (a) P02 in the earlier decade, (b) P02 in the recent decade, (c) P16 in the earlier decade, and (d) P16 in the recent decade. Grey lines are isoneutral surfaces of the labeled γ^N .

reflect limitations inherent on the eMLR or ensemble eMLR method generally. We assume that this error is uncorrelated between our 16 regression property combinations and that it therefore becomes a factor of 4 smaller for ensemble eMLR after averaging our 16 sets of results.

We estimate the final source of error attributable to other inadequacies of the eMLR method in Appendix B, where we find a reconstruction error of $0.55 \pm 2.6 \mu\text{mol kg}^{-1}$ (mean \pm RMSE) for simulated property distributions with no measurement errors. We call this the minimum error or e_{min} . This e_{min} estimate reflects an unknown contribution from errors from source 2, as these errors also apply to reconstructions of simulated fields with nonstationary modes of variability.

Overall estimate errors (E , Figure A2) are estimated according to equation (A3) as follows:

$$E = \sqrt{\sum_{n=1}^6 e_n^2 + \left(\frac{S_{16}}{4}\right)^2} \quad (\text{A3})$$

We do not include e_{min} in this estimate because the average RMSE for individual ΔC_{anth} estimates ($\pm 3.5 \mu\text{mol kg}^{-1}$) obtained from equation (A3) is already larger than the average estimate we obtain from an independent approach to estimating overall RMSE ($\pm 2.7 \mu\text{mol kg}^{-1}$) in Appendix B. We therefore contend that the majority of e_{min} is accounted for by the perturbation analysis. In our figures estimates are considered significant in figures if they exceed 1.96 times the E specific to that estimate.

Extrapolation errors are potentially large for basin averages estimated from only a pair of hydrographic lines. Lateral tracer gradients resulting from gyre interior circulation pose an additional challenge for extrapolations from P16. However, a reconstruction of our estimates along P02 using the P16 section estimates had a RMSE of only $1 \mu\text{mol kg}^{-1}$ for both decades and 4% and 13% average errors in the early and later decades, respectively. Given these estimates and the $\sim 20\%$ E estimate from equation (A3), we assign our basin inventory change estimates uncertainties of 25% of the total value.

Appendix B: Assessing the Efficacy of Moving Windows and Ensemble eMLR Modifications

We test the efficacy of the ΔC_{bio} (step 2), moving windows (step 4), and ensemble eMLR (step 5) methodological modifications to eMLR for improving C_{anth} storage change estimates using Earth System Model output with known C_{anth} changes. We use a pair of simulations of ocean biogeochemistry with the coupled Earth System Model (ESM2M) developed at the National Oceanic and Atmospheric Administration's Geophysical Fluid Dynamics Laboratory. The model consists of a 1° MOM4p1 ocean version [Griffies *et al.*, 2009] coupled to an approximately 2° version of the AM2 atmospheric model [Anderson *et al.*, 2004]. Ocean biogeochemistry is modeled with version 2 of the Tracers of Ocean Plankton with Allometric Zooplankton (TOPAZ2) biogeochemical model [Dunne *et al.*, 2013].

We consider a perturbation study focusing on the behavior of the TOAPZ2 model in ESM2M that was first presented by Carter *et al.* [2016b]. This specific perturbation study meets our scientific needs as it is based on a concentration-pathway configuration of the model and allows for a simple definition of C_{anth} . The model was spun-up under preindustrial atmospheric CO_2 boundary conditions for more than 1000 model years to minimize drift. Subsequent to the spin-up, the model was run for an additional 70 years with preindustrial boundary conditions for CO_2 as seen by the atmospheric radiation code. Over this same 70 year interval, two instances of the full TOPAZ2 biogeochemical model were run concurrently online. The first instance of TOPAZ2 maintained a constant preindustrial CO_2 boundary condition, while the second imposed a 1% year⁻¹ increase in the atmospheric boundary condition for CO_2 , such that it achieved doubling after approximately 70 years. As such, the difference in the carbon state variables as they evolve at each time step between the two TOPAZ2 instances of the 70 year period serves as our definition of C_{anth} . With identical ocean circulation, the C_T disparity that evolves over these 70 years is thereby attributable to C_{anth} storage. We use ensemble eMLR to reconstruct these C_T changes from model year 1995 to 2005 along five meridional sections from 90°S to 60°N along 179.5°E, 79.5°E, 59.5°E, 24.5°W, and 95.5°W between 150 and 1000 m depth. We then determine the mean and RMS errors along each section. Finally, we average the absolute values of these errors. We repeat this test with and without latitudinal restrictions on the moving windows, depth/density restrictions on the moving windows, and ensemble averaging.

A second set of tests is conducted using model outputs that have been perturbed to simulate measurement inaccuracies and imprecisions. We apply two sets of simulated errors to represent these sources of uncertainty. First, we perturb each simulated property value by applying a random offset selected from a normally distributed population with a mean of 0 and a standard deviation equal to the values given in the first row of Table B1 (representing measurement imprecisions). Second, we apply an offset that is identical for all measurements of a given parameter (representing measurement inaccuracy) using standard deviations from the second row in Table B1. The standard deviations for θ and S for this second set of perturbations are large because they also represent potential unresolved unmodeled shifts in the relationships between properties (see Appendix A, error source 2). We repeat this process 20 times for each of our five sections, creating a population of 100 realizations of the simulated parameter fields with simulated measurement errors. We then analyze these 100 realizations using traditional and ensemble eMLR and repeat our assessment as before. We also analyze these simulated fields with and without the ΔC_{bio} adjustment in equation (8).

The skill of the technique within these sets of simulations is shown in Table B2. We find that the mean error increases by 30–40% when a single regression is used in place of the ensemble mean, while the RMSE increases nearly twice this amount. Omitting the moving window in latitude leads to a small ~10% improvement in mean error, while omitting the moving window in density or depth doubles the mean error (though it is likely the common practice of using multiple regressions for various depth/density ranges works as well as a moving window). Neither window has a strong impact on the RMSE when the ensemble approach is used. Omitting the ΔC_{bio} adjustment increases the ensemble mean error and the RMSE by ~7–15%. This

Table B1. Standard Deviations of Normally Distributed Populations of Offsets Applied to Simulated Measurements

Offset	Error Type Represented	θ (°C)	S	C_T ($\mu\text{mol kg}^{-1}$)	AOU ($\mu\text{mol kg}^{-1}$)	N ($\mu\text{mol kg}^{-1}$)	Si ($\mu\text{mol kg}^{-1}$)
1	Imprecision	0.002	0.002	2	2	0.1	0.1
2	Inaccuracies or shifts	0.01	0.01	1	1	0.4	0.4

Table B2. Mean Error or Bias \pm RMSE in $\mu\text{mol kg}^{-1}$ for eMLR Reconstructions of C_{anth} Changes in Seawater Deeper Than 150 m Depth Between 1995 and 2005 Along Five Meridional Transects in the ESM2M^a

	Ensemble	Nonensemble
No modifications	0.55 \pm 2.6	0.73 \pm 4.6
∞ Latitude window	0.60 \pm 2.7	1.31 \pm 5.3
∞ Depth/density window	1.10 \pm 2.5	1.50 \pm 4.6
+ Simulated errors	1.45 \pm 2.7	2.02 \pm 4.4
+ Simulated errors, no ΔC_{bio}	1.67 \pm 2.9	2.50 \pm 4.8

^aColumns correspond to analyses done with and without ensemble averaging.

analysis suggests that the overall error with our approach with measurement uncertainties is $1.45 \pm 2.7 \mu\text{mol kg}^{-1}$ (mean \pm RMSE.), which is smaller than the estimates in Appendix A and likely represents a best-case scenario with little mesoscale variability and an even measurement grid. Except when noted, errors in presented in this manuscript are the errors estimated in Appendix A.

OA-related biogeochemical C_T redistribution slightly complicates our use of simulated C_T changes as a ΔC_{anth} benchmark because it is a process affecting C_T distributions other than C_{anth} storage [Carter *et al.*, 2016b]. This redistribution may or may not be removed by subtracting regression coefficients during eMLR. Nevertheless, these changes are at most a small portion of the overall C_T changes: using the ΔAlk^* metric of Carter *et al.* [2016b] to quantify the impact of these changes reveals that $0.08 \pm 0.4 \mu\text{mol kg}^{-1} A_T$ (mean \pm RMSE) change can be attributed to these feedbacks over our study area. This small A_T redistribution would result in an even smaller C_T redistribution from solubility changes or changed activity of the hard tissue pump.

Acknowledgments

All data used can be accessed at <http://cchdo.ucsd.edu/>. Anthropogenic carbon estimates generated in this research are available as a supplement. This research would not be possible without the hard work of the scientists and crew aboard the R/Vs *Revelle*, *Palmer*, *Brown*, *Discoverer*, *Washington*, *Thompson*, *Knorr*, and *Kaiyo-Maru*. We thank funding agencies and program managers as follows: B.R.C. was supported by the Carbon Data Management and Synthesis NOAA grant (N8R1SE3-PGC) managed by Kathy Tedesco. A.M.M. was supported by NOAA grant NA11OAR4310063. The support of K.B.R. comes through awards NA17RJ2612 and A08OAR4320752, including support through the NOAA Office of Climate Observations, NOAA award NA11OAR4310066. This is PMEL contribution 4519 and JISAO contribution 2016-01-22.

References

- Amaya, D., N. E. Bond, J. A. Miller, and M. J. DeFlorio (2016), The evolution and known atmospheric forcing mechanisms behind the 2013–2015 North Pacific warm anomalies, *US CLIVAR Var. Newsl.*, *14*(2), 1–6.
- Anderson, J. L., et al. (2004), The new GFDL global atmosphere and land model AM2-LM2: Evaluation with prescribed SST simulations, *J. Climate*, *17*, 4641–4673.
- Anderson, L. A., and J. L. Sarmiento (1994), Redfield ratios of remineralization determined by nutrient data analysis, *Global Biogeochem. Cycles*, *8*(1), 65–80, doi:10.1029/93GB03318.
- Böning, C. W., A. Disper, M. Visbeck, S. R. Rintoul, and F. U. Schwarzkopf (2008), The response of the Antarctic Circumpolar Current to recent climate change, *Nat. Geosci.*, *1*, 864–869, doi:10.1038/ngeo362.
- Broecker, W. S. (1974), “NO”, a conservative water-mass tracer, *Earth Planet. Sci. Lett.*, *23*(1), 100–107, doi:10.1016/0012-821X(74)90036-3.
- Canadell, J. G., C. Le Quéré, M. R. Raupach, C. B. Field, E. T. Buitenhuis, P. Ciais, T. J. Conway, N. P. Gillett, R. A. Houghton, and G. Marland (2007), Contributions to accelerating atmospheric CO₂ growth from economic activity, carbon intensity, and efficiency of natural sinks, *Proc. Natl. Acad. Sci. U.S.A.*, *104*, 18,866–70, doi:10.1073/pnas.0702737104.
- Carter, B. R., J. R. Toggweiler, R. M. Key, and J. L. Sarmiento (2014), Processes determining the marine alkalinity and calcium carbonate saturation state distributions, *Biogeosciences*, *11*(24), 7349–7362, doi:10.5194/bg-11-7349-2014.
- Carter, B. R., N. L. Williams, A. R. Gray, and R. A. Feely (2016a), Locally interpolated alkalinity regression for global alkalinity estimation, *Limnol. Oceanogr. Methods*, *14*(4), 268–277, doi:10.1002/lom3.10087.
- Carter, B. R., T. L. Frölicher, J. P. Dunne, K. B. Rodgers, R. D. Slater, and J. L. Sarmiento (2016b), When can ocean acidification impacts be detected from decadal alkalinity measurements?, *Global Biogeochem. Cycles*, *30*(4), 595–612, doi:10.1002/2015GB005308.
- Chu, S. N., Z. A. Wang, S. C. Doney, G. L. Lawson, and K. A. Hoering (2016), Changes in anthropogenic carbon storage in the Northeast Pacific in the last decade, *J. Geophys. Res. Ocean.*, doi:10.1002/2016JC011775.
- Deutsch, C., S. Emerson, and L. Thompson (2006), Physical-biological interactions in North Pacific oxygen variability, *J. Geophys. Res.*, *111*, C09S90, doi:10.1029/2005JC003179.
- Dickson, A. G., and F. J. Millero (1987), A comparison of the equilibrium constants for the dissociation of carbonic acid in seawater media, *Deep Sea Res. Part A. Oceanogr. Res. Pap.*, *34*(10), 1733–1743, doi:10.1016/0198-0149(87)90021-5.
- Doney, S. C., V. J. Fabry, R. A. Feely, and J. A. Kleypas (2009), Ocean acidification: The other CO₂ problem, *Ann. Rev. Mar. Sci.*, *1*, 169–92, doi:10.1146/annurev.marine.010908.163834.
- Dunne, J. P., et al. (2013), GFDL’s ESM2 Global Coupled Climate–Carbon Earth System Models. Part II: Carbon system formulation and baseline simulation characteristics, *J. Climate*, *26*(7), 2247–2267, doi:10.1175/JCLI-D-12-00150.1.
- Durack, P. J., S. E. Wijffels, and R. J. Matear (2012), Ocean salinities reveal strong global water cycle intensification during 1950 to 2000, *Science*, *336*, 455–8, doi:10.1126/science.1212222.
- Emerson, S., Y. W. Watanabe, T. Ono, and S. Mecking (2004), Temporal trends in apparent oxygen utilization in the upper pycnocline of the North Pacific: 1980–2000, *J. Oceanogr.*, *60*, 139–147, doi:10.1023/B:JOCE.0000038323.62130.a0.
- England, M. H., S. McGregor, P. Spence, G. A. Meehl, A. Timmermann, W. Cai, A. Sen Gupta, M. J. McPhaden, A. Purich, and A. Santoso (2014), Recent intensification of wind-driven circulation in the Pacific and the ongoing warming hiatus, *Nat. Clim. Chang.*, *4*(3), 222–227, doi:10.1038/nclimate2106.
- Feely, R. A., C. L. Sabine, R. H. Byrne, F. J. Millero, A. G. Dickson, R. Wanninkhof, A. Murata, L. A. Miller, and D. Greeley (2012), Decadal changes in the aragonite and calcite saturation state of the Pacific Ocean, *Global Biogeochem. Cycles*, *26*, doi:10.1029/2011GB004157.
- Feely, R., S. Doney, and S. Cooley (2009), Ocean acidification: Present conditions and future changes in a High-CO₂ world, *Oceanography*, *22*, 36–47, doi:10.5670/oceanog.2009.95.
- Friis, K., A. Körtzinger, J. Pätsch, and D. W. R. Wallace (2005), On the temporal increase of anthropogenic CO₂ in the subpolar North Atlantic, *Deep Sea Res. Part I Oceanogr. Res. Pap.*, *52*, 681–698, doi:10.1016/j.dsr.2004.11.017.

- Gattuso, J. P., and R. A. Feely (2016), *Future of the Ocean and its Seas: A Non-governmental Scientific Perspective on Seven Marine Research Issues of G7 Interest*, pp. 24–28, CSU-IAPSO-IUGG-SCOR, Paris.
- Gattuso, J.-P., et al. (2015), OCEANOGRAPHY. Contrasting futures for ocean and society from different anthropogenic CO₂ emissions scenarios, *Science*, 349(6243aac4722), doi:10.1126/science.aac4722.
- Gebbie, G., and P. Huybers (2012), The mean age of ocean waters inferred from radiocarbon observations: Sensitivity to surface sources and accounting for mixing histories, *J. Phys. Oceanogr.*, 42, 291–305, doi:10.1175/JPO-D-11-043.1.
- Goodkin, N. F., N. M. Levine, S. C. Doney, and R. Wanninkhof (2011), Impacts of temporal CO₂ and climate trends on the detection of ocean anthropogenic CO₂ accumulation, *Global Biogeochem. Cycles*, 25, GB3023, doi:10.1029/2010GB004009.
- Griffies, S., M. Schmidt, and M. Herzfeld (2009), *Elements of MOM4P1*, Princeton, N. J.
- Hanawa, K., and L. Talley (2001), Mode waters, *Int. Geophys. Ser.*
- Jackett, D. R., and T. J. McDougall (1997), A neutral density variable for the world's oceans, *J. Phys. Oceanogr.*, 27(2), 237–263, doi:10.1175/1520-0485(1997)027<0237:ANDVFT>2.0.CO;2.
- Keeling, C. D. (1986), *Atmospheric CO₂ Concentrations—Mauna Loa Observatory, Hawaii 1958–1986*, Oak Ridge National Laboratory.
- Key, R. M., A. Kozyr, C. L. Sabine, K. Lee, R. Wanninkhof, J. L. Bullister, R. A. Feely, F. J. Millero, C. Mordy, and T.-H. Peng (2004), A global ocean carbon climatology: Results from Global Data Analysis Project (GLODAP), *Global Biogeochem. Cycles*, 18, 1–23, doi:10.1029/2004GB002247.
- Khatiwalala, S., F. Primeau, and T. Hall (2009), Reconstruction of the history of anthropogenic CO₂ concentrations in the ocean, *Nature*, 462, 346–9, doi:10.1038/nature08526.
- Kouketsu, S., A. Murata, and T. Doi (2013), Decadal changes in dissolved inorganic carbon in the Pacific Ocean, *Global Biogeochem. Cycles*, 27, 65–76, doi:10.1029/2012GB004413.
- Le Quééré, C., R. Moriarty, R. M. Andrew, G. P. Peters, P. Ciais, P. Friedlingstein, and S. D. Jones (2015), Global carbon budget 2014, *Earth Syst. Sci. Data*, 7(1), 47–85, doi:10.5194/essd-7-47-2015.
- Levine, N. M., S. C. Doney, R. Wanninkhof, K. Lindsay, and I. Y. Fung (2008), Impact of ocean carbon system variability on the detection of temporal increases in anthropogenic CO₂, *J. Geophys. Res.*, 113, C03019, doi:10.1029/2007JC004153.
- Locarnini, R. A. et al. (2013), *World Ocean Atlas 2013. Vol. 1: Temperature*, edited by S. Levitus and A. Mishonov, NOAA Atlas NESDIS 73, 40 pp., doi:10.1182/blood-2011-06-357442.
- Matsumoto, K. (2007), Radiocarbon-based circulation age of the world oceans, *J. Geophys. Res.*, 112, C09004, doi:10.1029/2007JC004095.
- McPhaden, M. J., and D. Zhang (2002), Slowdown of the meridional overturning circulation in the upper Pacific Ocean, *Nature*, 415(6872), 603–608, doi:10.1038/415603a.
- McPhaden, M. J., and D. Zhang (2004), Pacific Ocean circulation rebounds, *Geophys. Res. Lett.*, 31, L18301, doi:10.1029/2004GL020727.
- Mecking, S., C. Langdon, R. A. Feely, C. L. Sabine, C. A. Deutsch, and D.-H. Min (2008), Climate variability in the North Pacific thermocline diagnosed from oxygen measurements: An update based on the U.S. CLIVAR/CO₂ Repeat Hydrography cruises, *Global Biogeochem. Cycles*, 22, 1–11, doi:10.1029/2007GB003101.
- Morgan, P., and L. Pender (2006), CSIRO Marine Research MATLAB Seawater Software Library. [Available at http://www.marine.csiro.au/marq/edd_search.Browse_Citation?txtSession=6438&brief=Y (Accessed 12 March 2016).]
- Murata, A., Y. Kumamoto, S. Watanabe, and M. Fukasawa (2007), Decadal increases of anthropogenic CO₂ in the South Pacific subtropical ocean along 32°S, *J. Geophys. Res.*, 112, C05033, doi:10.1029/2005JC003405.
- Nakano, H., M. Ishii, K. B. Rodgers, H. Tsujino, and G. Yamanaka (2015), Anthropogenic CO₂ uptake, transport, storage, and dynamical controls in the ocean imposed by the meridional overturning circulation: A modeling study, *Global Biogeochem. Cycles*, 29, 1706–1724, doi:10.1002/2015GB005128.
- Pfister, C. A., et al. (2014), Detecting the unexpected: A research framework for ocean acidification, *Environ. Sci. Technol.*, 48(17), 9982–94, doi:10.1021/es501936p.
- Plancherel, Y., K. Rodgers, R. Key, A. Jacobson, and J. Sarmiento (2013), Role of regression model selection and station distribution on the estimation of oceanic anthropogenic carbon change by eMLR, *Biogeosciences*, 10(7), 4801–4831, doi:10.5194/bg-10-4801-2013.
- Purkey, S. G., and G. C. Johnson (2010), Warming of global abyssal and deep southern ocean waters between the 1990s and 2000s: Contributions to global heat and sea level rise budgets, *J. Climate*, 23, 6336–6351, doi:10.1175/2010JCLI3682.1.
- Purkey, S. G., and G. C. Johnson (2013), Antarctic bottom water warming and freshening: Contributions to sea level rise, ocean freshwater budgets, and global heat gain, *J. Climate*, 26(16), 6105–6122, doi:10.1175/JCLI-D-12-00834.1.
- Sabine, C. L., R. A. Feely, R. M. Key, J. L. Bullister, F. J. Millero, K. Lee, T.-H. Peng, B. Tilbrook, T. Ono, and C. S. Wong (2002), Distribution of anthropogenic CO₂ in the Pacific Ocean, *Global Biogeochem. Cycles*, 16, 30–1–30–17, doi:10.1029/2001GB001639.
- Sabine, C. L., et al. (2004), The oceanic sink for anthropogenic CO₂, *Science*, 305(5682), 367–71, doi:10.1126/science.1097403.
- Sabine, C. L., R. A. Feely, F. J. Millero, A. G. Dickson, C. Langdon, S. Mecking, and D. Greeley (2008), Decadal changes in Pacific carbon, *J. Geophys. Res.*, 113, C07021, doi:10.1029/2007JC004577.
- Talley, L. D. (1993), Distribution and formation of North Pacific Intermediate Water, *J. Phys. Oceanogr.*, 23(3), 517–537, doi:10.1175/1520-0485(1993)023<0517:DAFONP>2.0.CO;2.
- Velo, A., F. F. Pérez, T. Tanhua, M. Gilcoto, A. F. Ríos, and R. M. Key (2013), Total alkalinity estimation using MLR and neural network techniques, *J. Mar. Syst.*, 111–112, 11–18, doi:10.1016/j.jmarsys.2012.09.002.
- Wallace, D. (1995), *Monitoring Global Ocean Carbon Inventories*, College Station, Tex.
- Wanninkhof, R., S. C. Doney, J. L. Bullister, N. M. Levine, M. Warner, and N. Gruber (2010), Detecting anthropogenic CO₂ changes in the interior Atlantic Ocean between 1989 and 2005, *J. Geophys. Res.*, 115, C11028, doi:10.1029/2010JC006251.
- Waugh, D. W., T. M. Hall, B. I. McNeil, R. Key, and R. J. Matear (2006), Anthropogenic CO₂ in the oceans estimated using transit time distributions, *Tellus B*, 58, 376–389, doi:10.1111/j.1600-0889.2006.00222.x.
- Waugh, D. W., et al. (2013), Recent changes in the ventilation of the southern oceans, *Science*, 339(6119), 568–70, doi:10.1126/science.1225411.
- Williams, N. L., R. A. Feely, C. L. Sabine, A. G. Dickson, J. H. Swift, L. D. Talley, and J. L. Russell (2015), Quantifying anthropogenic carbon inventory changes in the Pacific sector of the southern ocean, *Mar. Chem.*, 174, 147–160, doi:10.1016/j.marchem.2015.06.015.
- Woolsey, R. J., F. J. Millero, and R. Wanninkhof (2016), Rapid anthropogenic changes in CO₂ and pH in the Atlantic Ocean: 2003–2014, *Global Biogeochem. Cycles*, 30, 1–21, doi:10.1002/2015GB005248.
- Yasuda, I. (1997), The origin of the North Pacific Intermediate Water, *J. Geophys. Res. Ocean.*, 102(C1), 893–909, doi:10.1029/96JC02938.
- Zweng, M. M., et al. (2013), *World Ocean Atlas 2013, Volume 2: Salinity*, edited by S. Levitus and A. Mishonov, 39 pp., Washington, D. C.